ABSTRACT

DHRIMAJ, HELION. An Evaluation of Switched and Synchronous Reluctance Machines for Electric Power Steering Application. (Under the direction of Dr. Iqbal Husain).

The research paper covers the fundamentals and analysis of a Switched Reluctance Machine (SRM) designed and constructed of the SRM for automotive electric power steering (EPS) application. The SRM under evaluation was built through a previous project where a predictive current control algorithm was implemented in the micro-controller code with the aim of lowering torque ripple. Starting with a discussion on experiments performed in previous research, this paper continues with simulation and experimental analysis for extensive performance evaluation of the SRM. Experimental data with poor torque performance is analyzed and the results are explained. An analysis of the key parameters is carried out to measure their effects on torque performance. The root cause for poor torque ripple performance in a second similarly constructed SRM were evaluated and identified. Lastly, a Synchronous Reluctance Machine (SynRM) model is designed and simulated for automotive EPS application to overcome the inherent torque ripple issues associated with SRMs. In compliance with the SRM criteria, the SynRM simulation results show good torque ripple performance for EPS application.

An Evaluation of Switched and Synchronous Reluctance Machines for Electric Power Steering Application

by
Helion Dhrimaj

A thesis submitted to the Graduate Faculty of
North Carolina State University
in partial fulfillment of the
requirements for the degree of
Masters of Science

Electrical Engineering

Raleigh, North Carolina

2016

APPROVED BY:

_____
Dr. Iqbal Husain
Committee Chair

_____ _____
Dr. Srdjan Lukic Dr. Gregory D. Buckner

DEDICATION

Për mamin tim! (To my mom)

BIOGRAPHY

The author of this paper, Helion Dhrimaj, was raised in Tirana, Albania. Together with his family he moved to the United States at age 11. He developed an interest in the subjects of art, history, architecture, and technology. Helion chose to pursue a degree in engineering and hopes to work as an engineer after graduating.

ACKNOWLEDGMENTS

I would like to thank my professor, Dr. Iqbal Husain, for giving me the opportunity to pursue a thesis based Masters degree and become involved in this research project. I would also like to thank my friend Zhao Wan and the rest of my friends and colleagues in the electric machine design research group for their help and support.

TABLE OF CONTENTS

LIST OF TABLES

LIST OF FIGURES

Chapter 1 Introduction to SRM

1.1 History of Switched Reluctance Machine

The history of the switched reluctance machine (SRM) can be divided into two main eras. The first one covers the period prior to the implementation of the power transistor, micro-electronics, and computerized control [1] [2]. According to T.J.E. Miller, the earliest SRM was built in 1838 for the purposes of train propulsion in the Glasgow-Edinburgh railway. Other machine developments characterized as switched reluctance motors, occurred simultaneously in the late 1830's and early 1840's [3]. Figure 1 below shows an early SRM design with one rotor pole pair.

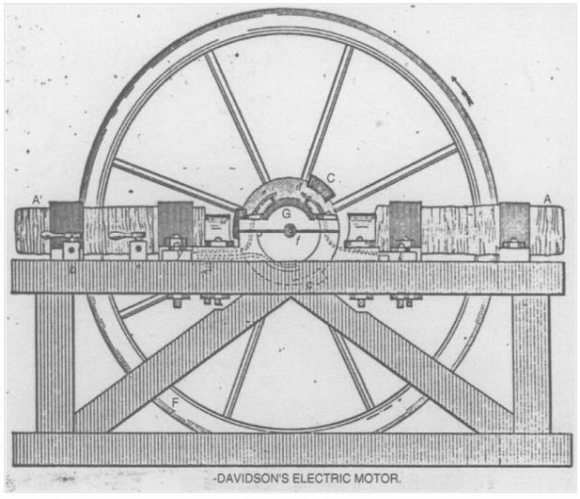

Figure 1: Davidson motor showing two electromagnets with opposite polarity and one of three armature bars on the rotor. [1]

Due to developments in other motor technologies, the SRM was mainly considered a "philosophical instrument-maker's toy" [1]. The evolution or "reinvention" of the SRM, occurred during the mid-1960's [3]. Four major simultaneous developments occurred that sparked this re-invention:

1) Power Transistor Development, initially BJTs, followed by MOSFETs and IGBTs.

2) Microprocessor development and digital integrated circuitry implementing control algorithms.

3) High speed computers capable of using numerical methods for finite element analysis purposes.

4) Expansion in variable speed electric-motors [1].

1.2 **SRM Fundamentals**

According to T.J.E. Miller, a reluctance motor is a machine in which torque is generated by the tendency of the unaligned moving part to move toward an aligned region. The movement occurs because the machine naturally realigns the rotor poles at a position where the reluctance is brought to a minimum while the stator coils are energized [1]. This is shown in Figure 2 as the rotor moves from an unaligned position with respect to the stator (right), to where the rotor is aligned with the stator (left). As the rotating part moves toward the region where the stator and rotor poles align, the inductance of the SRM maximizes as shown in the Figure 3. The principle of increased inductance and lowered reluctance applies to all switched reluctance machines.

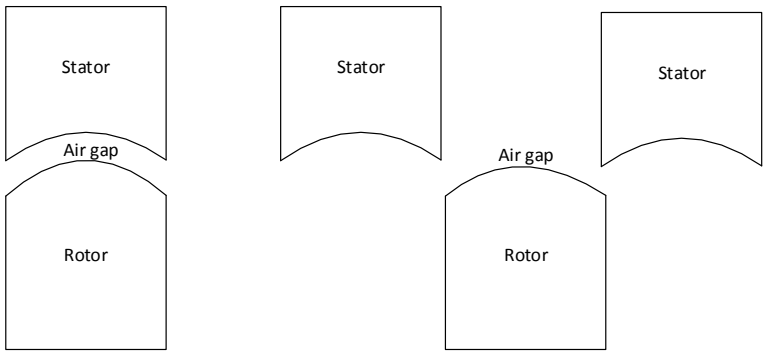

Figure 2: Aligned (left) and Unaligned (right) rotor position.

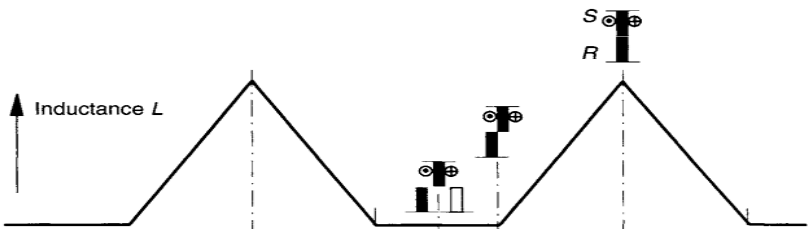

Figure 3: Maximum and minimum inductance dependent on the rotor position with respect to the stator [1].

1.2.1 **Equivalent Circuit Equations**

The voltage source V, is defined in equation 1 below. The phase resistance is described by R, the current by i, and the flux-linkage by λ.

$$\boldsymbol{V} = \boldsymbol{R} * \boldsymbol{i} + \frac{\boldsymbol{d}\,\boldsymbol{\lambda}(\boldsymbol{\theta},\boldsymbol{i})}{\boldsymbol{dt}} \qquad (\mathbf{1})$$

The flux linkage is dependent on the applied current and rotor position and is defined by equation 2, where L is the inductance.

$$\boldsymbol{\lambda}(\boldsymbol{\theta},\boldsymbol{i}) = \boldsymbol{L}(\boldsymbol{\theta},\boldsymbol{i}) * \boldsymbol{i} \quad (\mathbf{2})$$

Substituting the flux linkage into equation 1, the result is as written below:

$$\boldsymbol{V} = \boldsymbol{R} * \boldsymbol{i} + \frac{\boldsymbol{d}\,\boldsymbol{\lambda}(\boldsymbol{\theta},\boldsymbol{i})}{\boldsymbol{di}} * \frac{\boldsymbol{di}}{\boldsymbol{d}\,\boldsymbol{t}} + \frac{\boldsymbol{d}\boldsymbol{\lambda}(\boldsymbol{\theta},\boldsymbol{i})}{\boldsymbol{d}\boldsymbol{\theta}} * \frac{\boldsymbol{d}\boldsymbol{\theta}}{\boldsymbol{dt}} \qquad (\mathbf{3})$$

The last term in equation 3 is also referred to as the back-emf term or 'e'. At higher speeds the back-emf increases in magnitude thus reducing the amount of voltage available to meet the current rise demands.

Magnetic saturation in the SRM causes the flux linkage to maintain a nonlinear relationship with current and position. Figure 4 below presents a general relationship for the applied current and the flux linkage output, at various rotor positions.

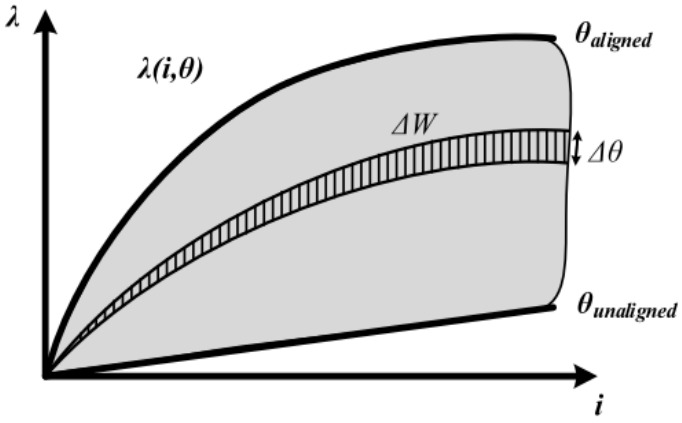

Figure 4: Flux-linkage (λ) with varying current (*i*) and position (θ). [4]

The co-energy is defined by equation 4 where Ψ is the flux linkage.

$$\boldsymbol{Wc} = \int \boldsymbol{\Psi} \boldsymbol{di} \qquad \mathbf{(4)}$$

Torque is the derivative of co-energy with respect to rotor position.

$$\boldsymbol{Te = \frac{\partial Wc}{\partial \theta}} \quad \textbf{(5)}$$

After subtracting the resistive losses and rate of change of magnetic stored energy from the input power, we are left with a linear equation describing torque:

$$\boldsymbol{Te = (1/2) * i^2 * \frac{dL}{d\theta}} \quad \textbf{(6)}$$

1.2.2 **Torque Production**

In the SRM, both the stator and rotor have salient poles, as seen in Figure 2 above with the 2/2 pole design. Torque is produced by the alignment tendency to minimize the reluctance by rotor pole re-alignment. Phase excitation permits the flow of current into the stator coils making it possible to control the torque production. Referring to equation 6, the torque output is dependent on the rise or fall of the inductance and the magnitude of the current applied to the coils. In order to generate positive motoring torque, phase currents must be applied while the inductance increases, i.e. as the rotor poles approach the aligned state. [1][2] In Figure 5 below, current is applied simultaneously with a rising inductance. Consequently, this causes the flux-linkage to increase as the maximum aligned position is reached, causing the production of positive or motoring torque. Negative or generating torque is generated if current flow is maintained simultaneously as the phase induction decreases, i.e. rotor moves away from the aligned position. If current supply is maintained during the rise and fall of the inductance, the net torque would sum up to zero. To avoid this, at the point where the inductance reaches the maximum point, current is ideally reduced to zero and is kept at this value throughout the negative motoring phase. As a result, the ideal current profile takes the form of a rectangular pulse shape.

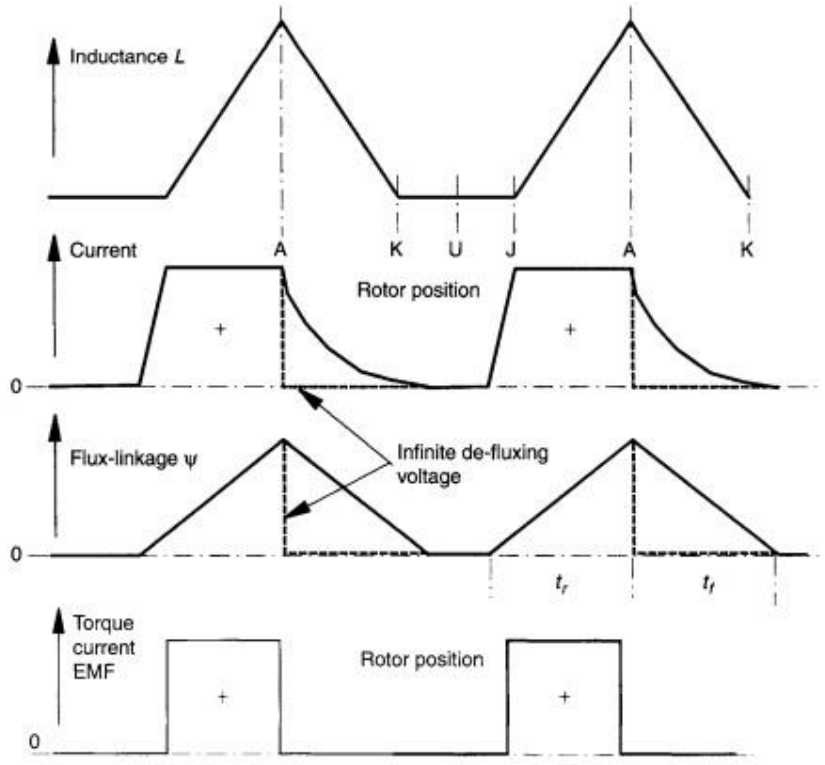

Figure 5: Positive motoring torque produced as result of current being applied while inductance increases. [1]

1.2.3 SRM Torque Ripple

At the point of commutation, defined as the point where the next phase conductor coil energizes while the established conductor coil de-energizes, the torque ripple occurs.

The torque ripple output is defined as:

$$\boldsymbol{Torque_{ripple}} = \frac{\boldsymbol{Torque_{max} - Torque_{min}}}{\boldsymbol{Torque_{Average}}} \quad (\mathbf{7})$$

As is shown in Figure 6 below, torque ripple is more noticeable where phase B ends and phase C reaches peak value. One possible way of reducing torque ripple is to properly shape the incoming and outgoing currents so that the individual torque contributions maintain a constant torque.

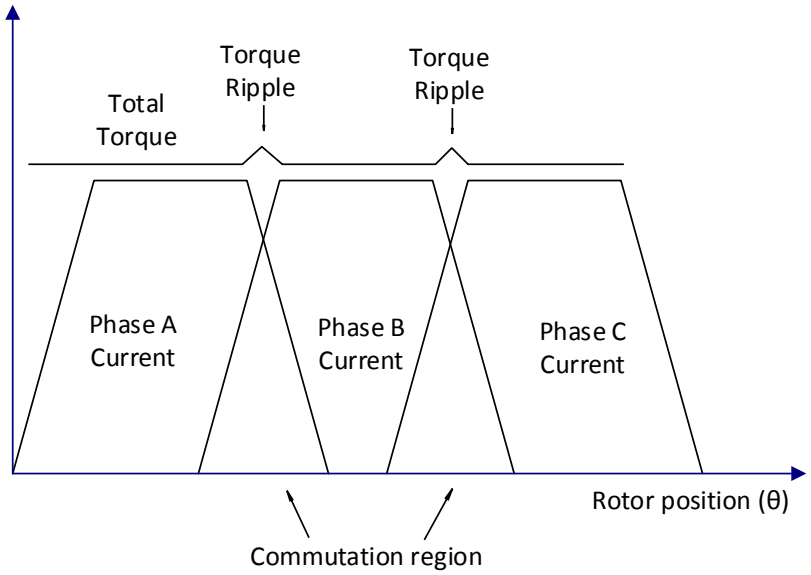

Figure 6: Torque ripple due to commutation of the phases ABC.

1.2.4 **Acoustic Noise**

In addition to torque ripple, SRMs also exhibit high levels of acoustic noise. This is a result of the radial forces on the SRM causing various mode shapes that lead to vibrations and ultimately acoustic noise. Depending on the SRM design, various types of modes that can occur in the SRM are shown below, in Figure 7.

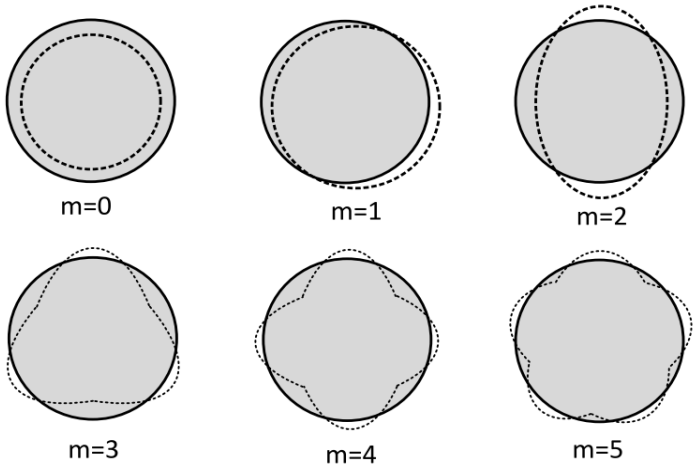

Figure 7: Various circumferential mode shapes of the SRM. [4]

1.3 **SRM Power Inverter**

The power inverter for the SRM has some features that are different from other multiphase motors. Each circuit phase in the SRM inverter operates independently. One of the reasons is to maintain phase current overlap to maintain constant torque. [4][5] In Figure 8 below, the three states of operation represented by one inverter phase are depicted in different colors. When the machine is functioning in positive motoring mode, the following operations occur:

- +VDC is applied to energize the coil while inductance increases.
- Zero voltage is applied (freewheeling) when there is sufficient time/position for de-energizing the coils.
- -VDC is applied to de-energize the coil in order to avoid generating torque.

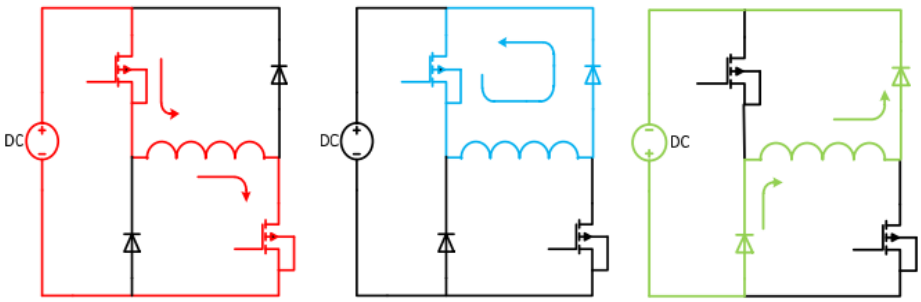

Figure 8: Classic bridge inverter when applied with: +VDC (red), 0 VDC (Blue), -VDC (Green). [4]

The SRM drive would only require one switch per phase winding since per torque production is phase independent. In case one of the phases experiences failure, operation continues. The SRM also maintains a switch in series with the phase winding that acts to delay an unexpected current rise in case of a shoot-through fault [2]. In order to apply bi-directional voltage 6 switches and 6 diodes are required which is more than conventional 6-switch inverters. Unlike conventional ac controllers and drives, each SRM controller and drive is usually designed for a particular application.

1.4 **SRM Operating Regions**

Like other motors, the SRM is designed with application suitable torque-speed specifications. Three regions define the torque-speed characteristics. In Figure 9 below the graphical representations of these three regions is shown.

Region one extends up to the base speed, ω_b. Base speed is defined as the maximum speed at which rated torque and maximum current can be maintained. As a result this region outputs constant torque.

In region two, the torque begins to fall linearly with increasing speed. With an increasing speed, the back-emf term also increases accordingly. At rotor speeds above ω_b, the region where the upcoming phase coil energizes is advanced. As a result, a smaller aligned area leads to less time for toque production and thus less torque output.

In the falling power region, or region three of the torque speed graph, the energizing of the pole conducting region cannot be advanced any further. With minimal time left for energizing the coils, the torque production falls even more rapidly.

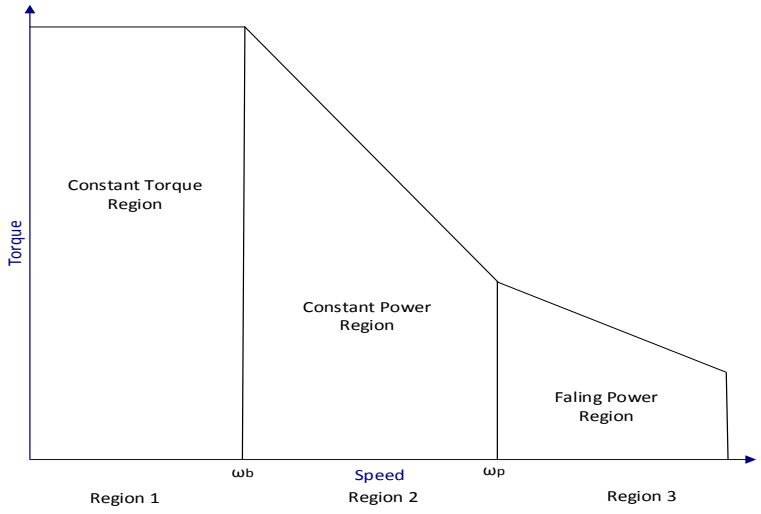

Figure 9: Torque speed characteristic for an SRM, highlighting the three important regions.

1.5 **Advantages and Disadvantages of SRM**

SRMs are generally known for their robustness and reliability. Requiring no magnets or brushes, they are simple and can be less expensive to construct. [5] Being a doubly salient machine, the downsides of the SRMs are their poor torque ripple performance as well as their high acoustic noise levels. To mitigate these issues, geometric changes to improve flux distribution can be made to the rotor and stator. For example, torque ripple decreases as the number of phases increase. [1][2] Furthermore, current shaping through effective current control algorithms can reduce torque ripple output as well as acoustic noise. The predictive current controller approach proposed by Rajib et. al is an excellent example of this [4]. In his research he implemented a predictive current controller to achieve low torque ripple for automotive electric power steering application.

The thesis is organized into five chapters as follows:

Chapter 1 Introduction to SRM

Chapter 1 introduces the SRM beginning with its history, followed by figures and equations describing the basic working principles. The advantages and disadvantages of the SRM are also discussed.

Chapter 2 SRM Evaluation for Automotive Power Steering

Chapter 2 discusses the previous work performed on two prototype SRMs, SRM-1 and SRM-2, designed for automotive power steering application. A summary of the SRM's specifications, design choices, subsequent experiments, as well as simulations are included. Furthermore, the experimental setup constructed in the previous research as well as the issues faced are discussed.

Chapter 3 Torque Ripple and Parameter Sensitivity Analysis

Chapter 3 introduces the results of SRM - 1's experiments findings. From the experimental results, issues encountered with the SRM's torque performance are analyzed in detail.

Using the SRMs simulation models, the effects of varying key parameters on torque performance are discussed.

Chapter 4 Synchronous Reluctance Machine Evaluation for EPS

Chapter 4 introduces a new synchronous reluctance machine design optimized for torque ripple performance. Based on previous requirements for automotive power steering machine design, the SynRM was modified and simulated in Finite Element Software, Flux2D. The results demonstrate the SynRM design was meets the requirements while maintaining application constraints.

Chapter 5 Conclusions

Discusses the shortfalls of the current SRM design, the advantages of a next generation synchronous reluctance machine, and further work remaining to more accurately compare the two machines for automotive EPS application.

Chapter 2 SRM for Automotive Power Steering

2.1 **Introduction to Electric Power Steering**

SRMs are generally viewed as machines that are robust and reliable but suffer from high torque ripple and acoustic noise emission [1],[2]. Electric Power Steering (EPS) machines require good torque ripple performance and low acoustic noise emission. In an EPS, the hydraulic components are replaced by an electric motor and accompanying gears. As feedback signals of torque, speed, and position are received, a torque command is given. The controller then applies the necessary voltage to the motor to match the desired torque command [6],[7]. Some benefits of using EPS over the conventional hydraulic steering are improved fuel economy, a simplified steering mechanism, a more easily tunable steering setup, as well as the absence of hydraulic fluids. Certain criteria that remains general to automotive EPS machine setup includes: fault tolerant machines, smooth-torque production (i.e. small ripple), good motor efficiency, and in case of mass production the ease of manufacturing [6].

2.2 **Motivation for SRM for EPS application**

SRMs can be an alternative for EPS systems. SRMs have low rotor inertia, no magnets or brushes, and no failures to cause unwanted torque in the off state [1]. When compared to a brushless DC motor for EPS application, the SRM fared better when both torque performance and cost were considered [8]. Due to existing issues, certain modifications must be made to the machine itself as well as its control algorithm. Geometric design modifications to the stator and rotor can improve the SRM torque ripple performance and reduce acoustic noise emission. In addition, a more efficient phase current switching algorithm can help lower torque ripple in commutation regions. In an earlier research, two SRMs with accompanying controller prototypes were designed and built for an automotive electric power steering application. The first prototype, SRM-1, being tuned and tested at North Carolina State University displayed good experimental and simulation results. The other prototype, the SRM-2, produced higher torque ripple.

The motivation behind this project is to develop a clear understanding of the sources of torque ripple through experimental data analysis. Furthermore to understand the effects of manufacturing and controller anomalies that lead to higher torque ripple in SRM, parameters of interest are varied. Lastly a next generation machine that manages the torque ripple sensitive parameters better is designed. The design objective is to provide the necessary torque output while improving on the torque ripple performance for vehicle power steering applications.

2.3 **SRM Characteristics**

2.3.1 **SRM Torque-Speed Characteristics**

The SRM design was based on the torque-speed requirements, as discussed in Chapter 1. Based on the application and subsequent criteria, a torque speed relation is developed. The SRM is designed with the torque-speed specifications shown in Figure 10 below. Looking at the torque speed relation in Figure 10, it is evident that the machine is designed for a rated torque output of 2.4 Nm. Furthermore, the machine is designed to operate at rated speed of 1000 rpm while maintaining 2.4-Nm torque output. The SRM reaches the no-load speed at 2200 rpm.

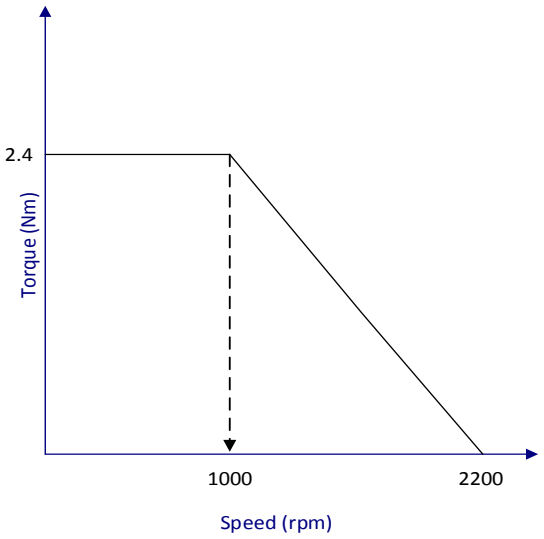

Figure 10: Torque-speed profile of SRM.

2.3.2 **T-i-θ profile**

The torque-current-position (T-i-θ) profile plays a crucial role in describing the machine characteristics. After the SRM is built based on the torque-speed specifications, the T-i-θ profile is extracted. In order to do so a single phase is excited with multiple current values. Assuming no pole to pole variation, one electrical cycle is sufficient to represent a full mechanical cycle profile. The rotor is swept over 45 degrees and the resulting multi-level torque T-i-θ profile is presented in Figure 11 below.

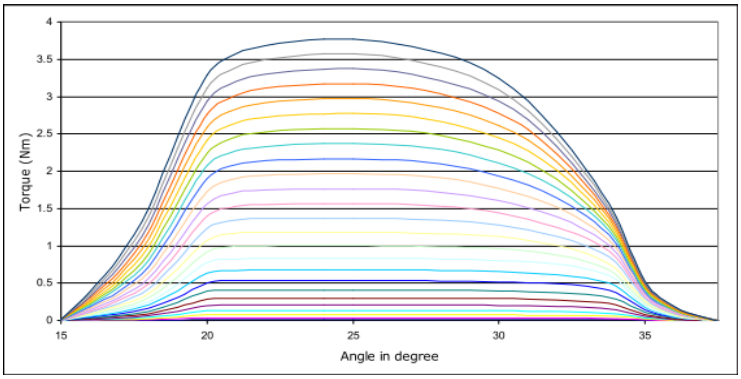

Figure 11: T-i-θ profile of SRM. [4]

2.3.3 **Current Profile**

Using the T-i-θ profiles, an initial current profile is generated for a specific torque level, in this case 1-Nm. In the simulation and experimental model, the torque feedback is used in many iterations in order to tune the shape of the current profile to maintain the ideal torque output. An example of the original as well as tuned current profile is shown in Figure 12 below.

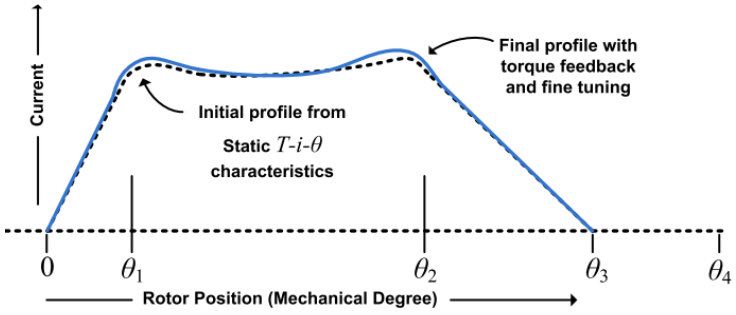

Figure 12: Initial and final current profile after fine-tuning with torque feedback. [4]

2.3.4 **Flux-Linkage Based Predictive Current Control**

Since phase commutation is mostly responsible for torque ripples, applying a good control algorithm can significantly improve torque performance. The previous work done on the SRM-1 introduced an offline predictive current control with a fixed switching frequency PWM implemented over the entire speed range [4]. Within the *k(th)* PWM cycle, the current and position values are measured. The voltage value to be applied for the *(k+1)th* cycle is calculated from a T-i-θ and λ-i-θ look up tables stored in the controller memory. The required voltage for the upcoming cycle is then described by equation (8).

$$V_{k+1} = \frac{3}{2}\left[\frac{iref_{k+2} + ik}{2} * R + \frac{\lambda(iref_{k+2},\ \theta_{est\,k+2}) - \lambda\,(ik,\theta k)}{2TP}\right] - \frac{Vk}{2} \quad (8)$$

2.3.5 **Coupled Simulation and Experimental Results**

Using the Finite Element Analysis (FEA) software Flux2D, as well as from the experiments performed in the lab, two separate λ-i-θ tables are derived. They correspond to the simulation model as well as the experimental model. Although the FEA model is an accurate representation of the physical machine, imperfections in manufacturing as well as differences in the built material influence the generated flux-linkage table. As a result, a unique λ-i-θ is implemented in the controller code, in the corresponding simulation and experimental model. The current outputs from experiments and simulations are shown in Figures 13 (a) and (b).

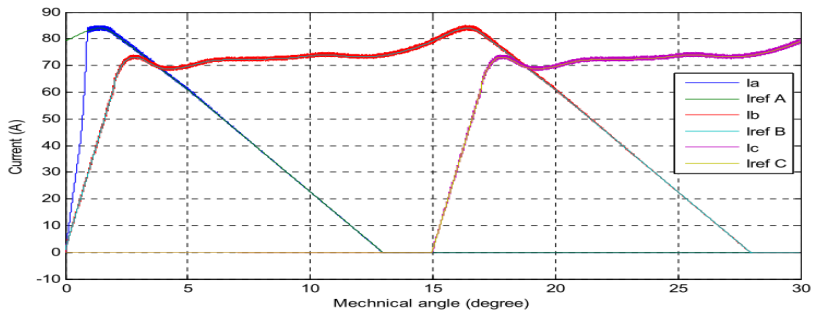

Figure 13 (a): Coupled simulation phase current and reference current at 100 rpm. [4]

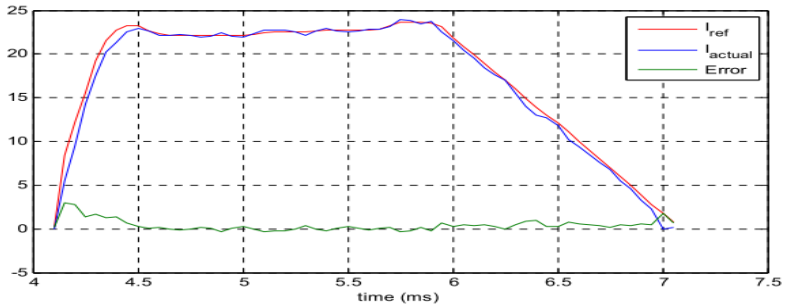

Figure 13 (b): Actual current and reference current from experimental run at 1500 rpm. [4]

2.3.6 **SRM Experimental Setup**

Illustration of the experimental setup available for SRM testing is shown in Figure 14 below.

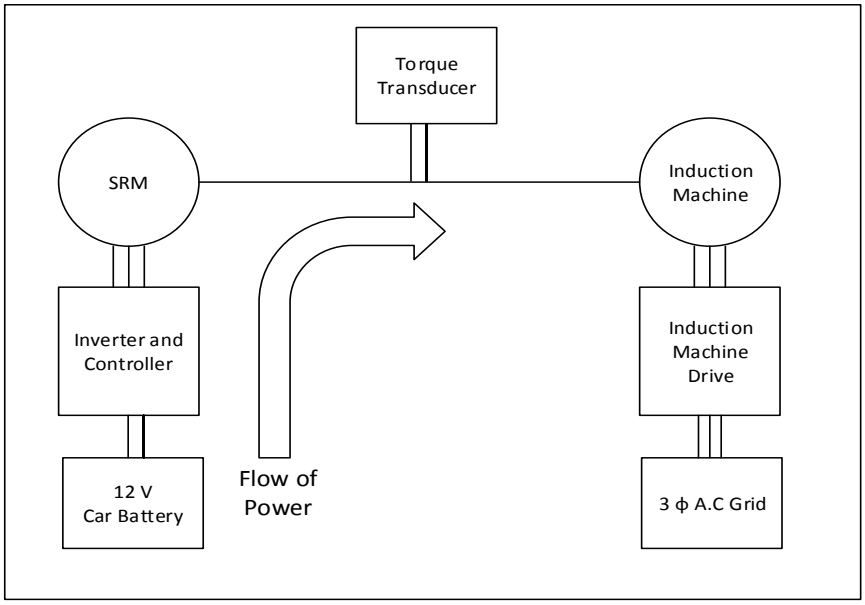

Figure 14: Experimental setup.

The picture in Figure 15(a) below shows the coupled equipment and test stand used for experimental testing. The supply for the SRM is a 12V car battery. The SRM is run in constant torque mode controlled by the inverter-controller module in Figure 15(b). The torque transducer has a low torque range but is accurate within that range. The dynamometer is an AC

Induction machine capable of operating as a 4-quadrant machine and is speed controlled through a commercial motor drive.

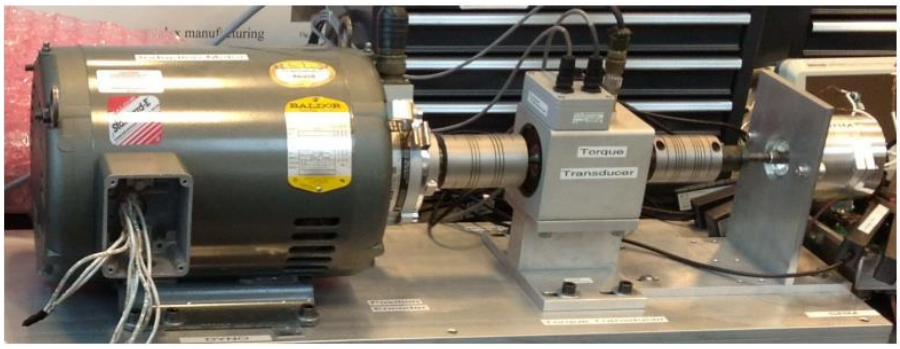

Figure 15 (a): From left to right: AC Induction dyno Torque transducer coupling – SRM. [4]

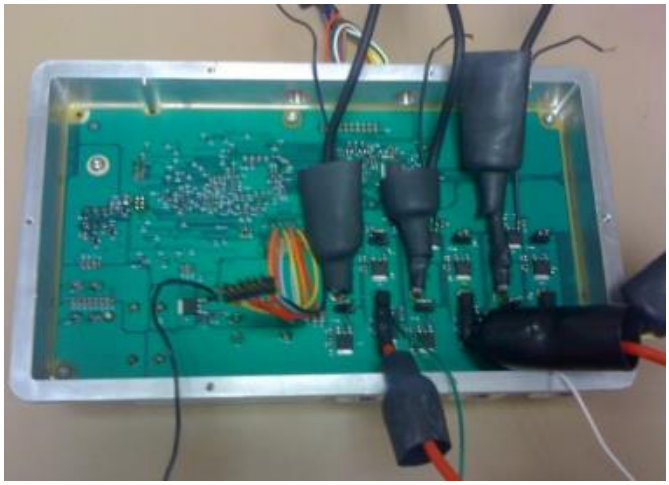

Figure 15 (b): SRM Inverter and controller module. [4]

2.4 **SRM Performance Issues**

The work done on the SRM to improve torque ripple performance showed acceptable results for EPS application. Less than 3% torque ripple was detected experimentally with the previously described motor design and controller setup. While the results were acceptable for the SRM-1 prototype, the same results could not be achieved for a similarly designed SRM, referred to as “SRM-2”.

2.4.1 **SRM-2 Experimental Setup**

Similar to the facilities at NCSU, the experimental setup for the SRM-2 included a 12V car battery connected to power inverter. The inverter was linked to the controller that was ultimately connected with the SRM. Several factors in the machine setup and experimental tests could act as additional sources of torque ripple. Based on experimental data and analysis, some of the errors found were:

1. Position Sensor Error
2. Phase Gain Variations
3. Poor Current Following at Higher Speeds

Further requirements from this project included understanding more on the effects of manufacturing imperfections as well as the effects of varying certain parameters; development of a multi-level torque profile for experimental purposes; fine tuning the simulation profile developed for simulation. The work performed on the theses challenges and requirements, is discussed in detail in Chapter 3.

2.4.2 **Position Sensor Error**

A two – pole analog resolver is used in the SRM to measure the rotor position and speed. The resolver consists of rotary transformers with primary and secondary windings. The secondary windings placed on the stator, are 90 degrees from each other. The primary winding on the rotor is excited and acts a reference signal to the secondary windings on the stator. Based on the signal strength ratio of the induced/reference signal, the position of the rotor is deduced. [9] Position accuracy can be affected by amplitude imbalance, quadrature error, inductance harmonics, reference phase shift, excitation signal distortion, and disturbance signal [10].

2.4.3 **Phase Gain Variation**

Another source of torque ripple is the current gain variation between the phases. Due to manufacturing imperfections, variations exist amongst different phases. Since the SRM permits individual phase excitation, each current command is controlled individually. As such,

each phase current is responsible for a portion of the total torque output. If an imbalance exists amongst the phase currents, an imbalanced torque contribution will occur that deteriorates the torque ripple performance. To compensate for variations, ideally each current phase gain should be tuned in order to produce the same amount of torque.

2.4.4 **Poor Current Following at Higher Speeds**

A number of factors could affect phase currents at higher speeds. The controller bandwidth, which is the ability to maintain good current following at all speeds, might limit current following performance. Some conventional controllers are designed and tuned with a desired bandwidth. Referring back to equation 3 in Chapter 1, the back-emf term also influences phase currents at higher speeds. Assuming the supply voltage remains constant and neglecting iron losses, the back-emf term increases linearly with speed. As a result the applied voltage for establishing motor current decreases accordingly. The rate of change of current is thus subject to the magnitude of the back-emf and as it becomes larger, the available voltage supply to meet the demands of the rate of change of current decreases. The result is a poorer following of the ideal reference current. Since torque is proportional to the square of the applied current, the torque ripple performance suffers as well. Equation 9 describes the relation between supply voltage, $back_{emf}$, and current.

$$V_D - R * i - \left(back_{emf}\right) = i\frac{dL}{dt} \quad (9)$$

2.4.5 **Manufacturing Imperfections and Parameter Sensitivity**

Manufacturing imperfections are inevitable. According to Fahimi et. al some SRM imperfections may include an imbalanced number of windings in the stator coils, lack of smoothness in the rotor poles, and rotor eccentricities issues [11]. In addition, temperature variation can influence machine operation and a fluctuating voltage supply may reduce the quality of operation. Rotor eccentricity imperfections and parametric analysis of phase resistances and voltage supply are discussed in more detail in Chapter 3.

Chapter 3 SRM Torque Ripple and Parametric Sensitivity Analysis

3.1 **Torque Ripple Analysis**

Torque ripple in the SRM-2 was found to be influenced from various contributing factors. Some major contributors can be roughly categorized into following categories:

1. **Position Sensor Error**
2. **Phase Gain Variation**
3. **Current Deterioration at Higher Speeds**
4. **System Resonance**

The remainder of the section describes in detail the effects of these errors, the challenges faced, as well as the approach taken to mitigate them. Experimental and simulation analysis were performed in the time and frequency domain. It is important to note that the frequency domain analysis was performed with respect to the fundamental frequency in revolutions per second. The 8^{th} and 16^{th} order harmonics with respect to the fundamental frequency, represent interphase variations since each phase conducts 8 times in 1 revolution. With three phases present, torque ripple due to phase commutation is detected in the 24^{th} and 48^{th} order harmonic.

3.1.1 **Position Sensor Error**

Position measurement error is a common problem for two-pole analog resolvers. To show the relationship between torque ripple and position sensor error, the torque output and phase currents were plotted and compared. Fig. 16 shows the poor torque ripple performance of the SRM with position sensor error. Figure 17 (a) shows the current profile when the position sensor error is small. In Figure 17 (b) the position sensor error is larger and so is the torque variation. An FFT analysis on this experimental data is shown in Figure 18. Sidebands of the 24^{th} order harmonic dominate, further suggesting an existing position sensor error.

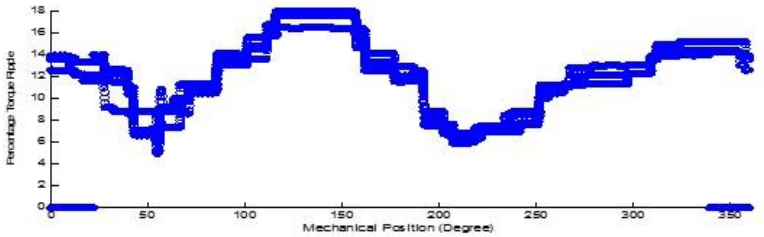

Fig. 16: Percentage torque ripple measured at 10 RPM with position sensor error present in the system.

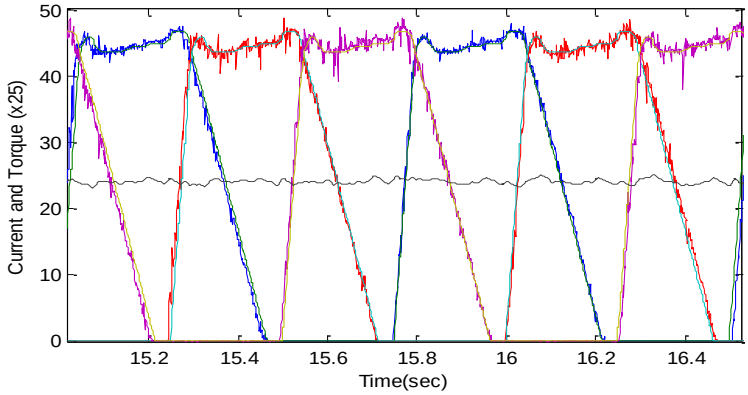

Figure 17 (a): Torque and phase current output plotted based on dyno and analog resolver position reading with small position error. (SRM, 10 RPM)

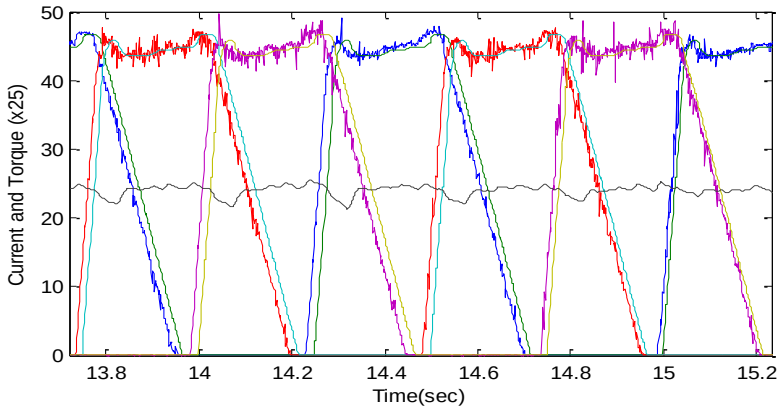

Figure 17 (b): Torque and phase current output plotted based on dyno and analog resolver position reading with large position error. (SRM, 10 RPM)

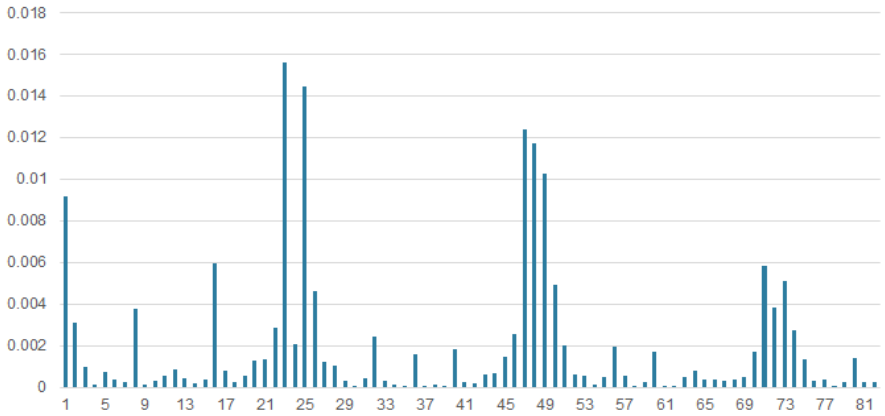

Figure 18: FFT of torque data from experimental tests conducted with SRM and SRM dyno.

An error correction technique was proposed and implemented. To compensate for the position error, first the readings from the analog position resolver were compared to that of a high resolution master encoder. Then to filter high frequency noise in the error profiles, several cycles of error data were collected and filtered using a median filter. The resulting position error profile shown in Figure 19 (a) was stored in a reference table with 1024 data points defining one mechanical cycle. During normal operation the referenced table value was added to the DSP position reading to instantaneously provide the SRM control code with corrected position data. The large spike was due to physical damage done to the sensor and was neglected for purpose of data analysis.

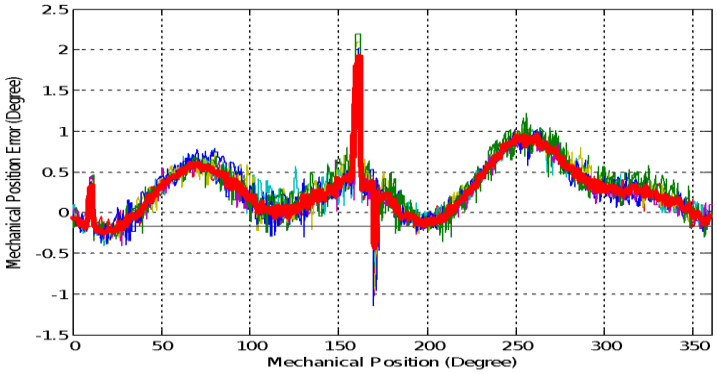

Figure 19 (a): Position sensor error for one mechanical cycle (several revolutions shown in different colors) from experimental tests conducted with SRM

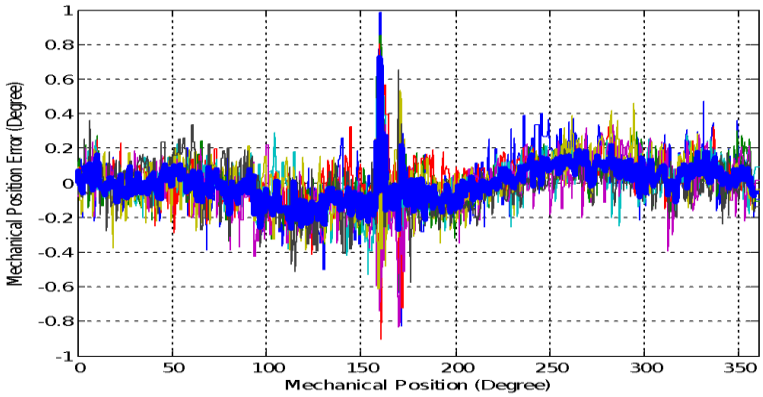

Figure 19 (b): Position error after correction from experimental tests conducted with SRM

After implementing the position error profile in the DSP code, the results depict a much smaller peak-to-peak mechanical position error in Figure 19 (b), less than 0.4 degree peak-to-peak. Further reductions in error is possible if more cycles of error data are collected to generate the error profile and a higher resolution table is used. In Figure 20 a much smaller torque ripple at the 24th order harmonic band can be observed. The biggest contributors to the torque ripple are now replaced by the 8th and 16th order harmonics. The 8th and 16th order harmonics arise from the phase to phase variation as well as current phase gain imbalance. Phase to phase variation is discussed next in more detail.

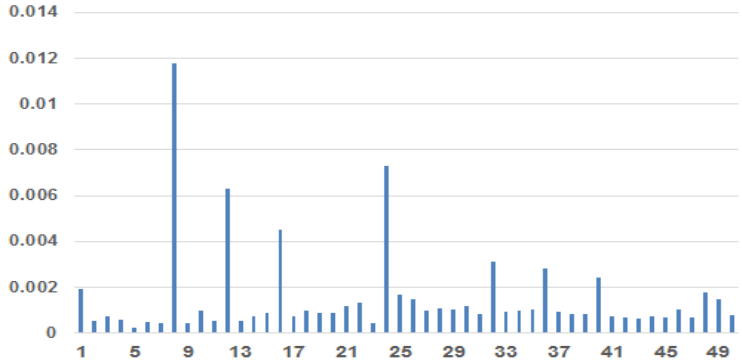

Figure 20: Torque ripple harmonics after position correction from experimental tests conducted with SRM.

3.1.2 **Phase Gain Variation**

Another source of error detected from experimental testing of the SRM-2 was the phase to phase variation. Because the SRM has 8 poles, each phase of the motor conducts 8 times in one revolution. Any 8th order torque ripple has to come from differences among the three phases. Simulation results in Figure 21 show that if phase A current is given a 5% gain difference with respect to phase B and C, 8th and 16th order harmonics will dominate in the torque ripple frequency plot.

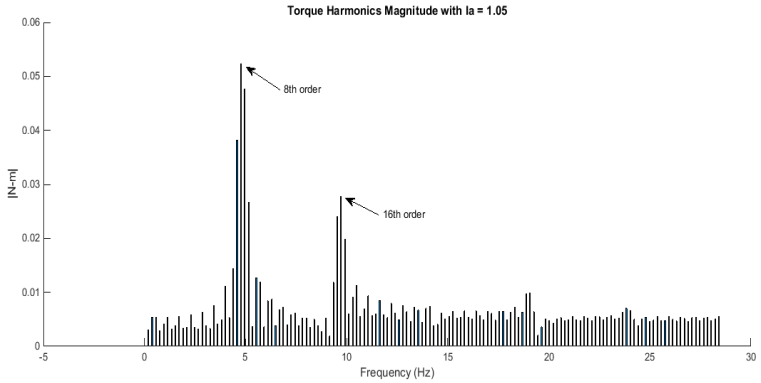

Figure 21: Simulation of torque ripple harmonics with phase variation from simulation.

The inter-phase variation can occur because of several reasons, including current sensor gain difference, phase resistance, and inductance difference due to machine construction. As a result, simply injecting equal currents in the three phases does not guarantee torque phase balance. The target for phase variation compensation is to individually change the current gain for each phase, such that the torque contribution from each phase is balanced as an end result.

To measure the torque output of each phase before any phase current gain adjustment, only one phase of the SRM is allowed to conduct current for each experiment. This experiment is conducted for each phase, then three single phase torques are plotted together in Figure 22 (a). It can be seen that the torque from phase C is noticeably larger than those of the other two phases. By taking the average torque from each phase, phase C average torque is 4% larger. However, the relationship between current and torque is nonlinear. So the process of tuning phase current gains will be an iterative process that will require repeated adjustments to the

gain and average torque comparisons. Proper balance of phase torque needs to be achieved in a few more iterations. The torque ripple frequency analysis after successful phase variation compensation shows clear reduction of 8th and 16th order harmonics in the simulation results in Figure 22 (b) in comparison to Figure 21.

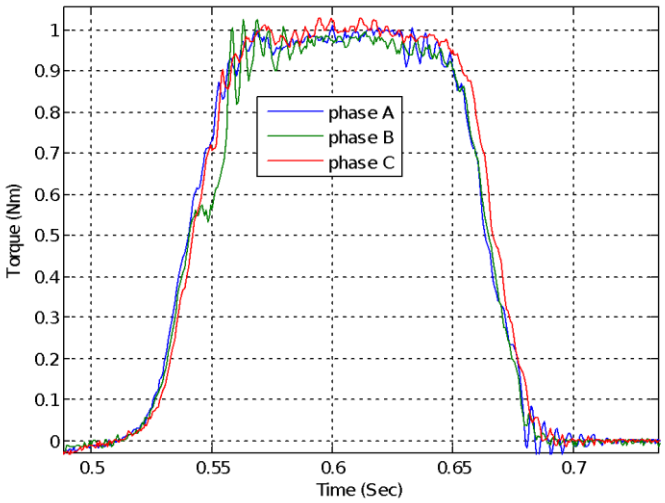

Figure 22 (a): Experimental results of single phase torques of the three phases. Tests conducted with SRM.

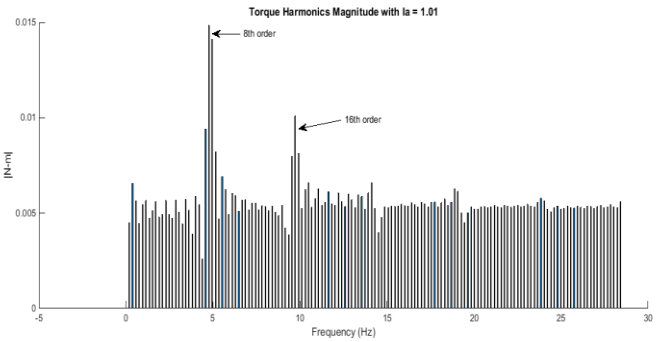

Figure 22 (b): Simulation results of torque ripple harmonics after phase variation compensation.

Torque output in the time domain after position correction and phase gain adjustment is plotted in Figure 23. Torque ripple output is within 5% when neglecting the large spikes due to position sensor damage.

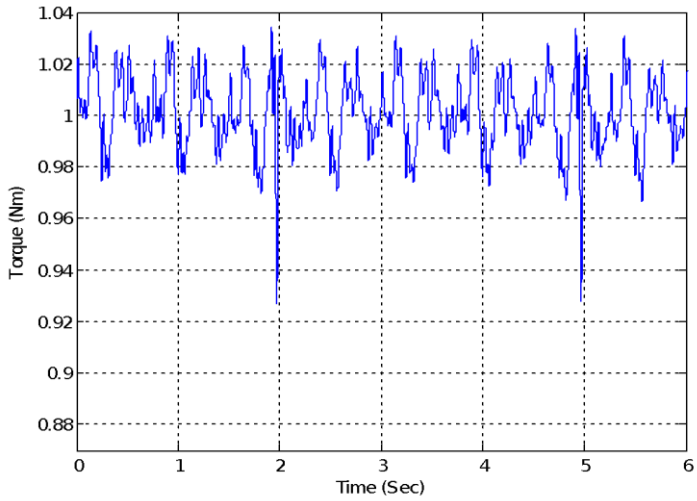

Figure 23: Output torque after phase variation correction, in 2 mechanical revolutions, from experimental tests conducted with SRM.

3.1.3 **Torque Ripple at Different Speeds**

After going through the error correction techniques described previously, torque ripple was measured at different speeds. The peak to peak ripple without position correction, measured over one mechanical cycle is shown in Figure 16**.** Since position sensor error was considered the major contributing factor, a good torque ripple performance is expected after the error correction. Comparing Figure 16 with Figure 24(a) it can be observed that there was significant improvement once the position correction profile was implemented. There was a small deterioration in the ripple performance as speed increases. After 50 RPM in Figure 24(b), a drastic rise in the peak to peak ripple is seen in Figures 24(c) and (d).

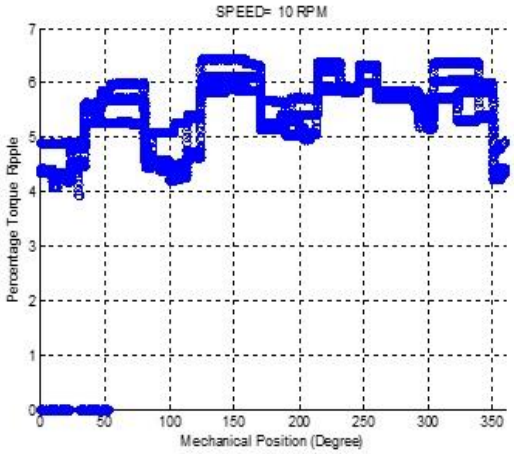

Figure 24 (a):Percentage torque ripple at 10 RPM (SRM)

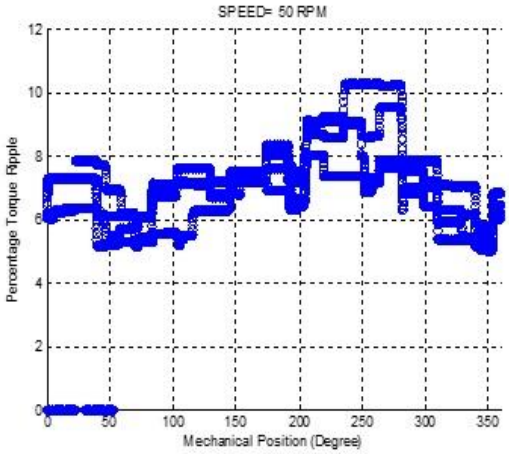

Figure 24 (b):Percentage torque ripple at 50 RPM (SRM)

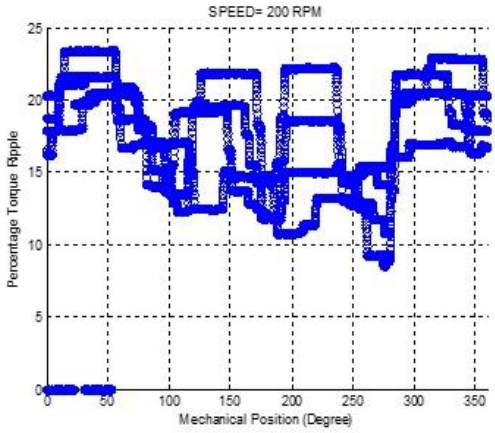

Figure 24 (c):Percentage torque ripple at 200 RPM (SRM)

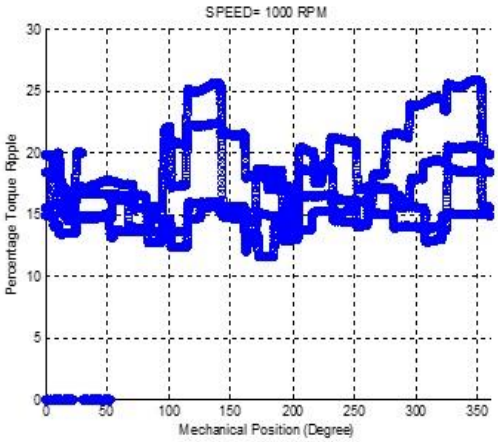

Figure 24 (d):Percentage torque ripple at 1000 RPM (SRM)

The controller implemented in the SRM is a model based predictive current controller. Due to this the bandwidth is not determined by its design. Instead the bandwidth is limited by the switching frequency which is 20 kHz. The mechanical and electrical frequencies are 40 Hz and 320 Hz respectively, so they are well within the bandwidth limitations. Controller bandwidth is not responsible for the poor current following at higher speeds.

At higher speed, the back EMF increases requiring higher DC bus voltage to maintain good current reference following. Larger torque ripple at higher speeds may mean that the controller

cannot follow the reference current, leading to poor torque performance. The current rise and current fall (slew rate) demands are described by equations 10 and 11 below.

$$\frac{di}{dt} = \frac{V_{dc} - \frac{d\lambda(i,\theta)}{d\theta}\omega - i * R}{L(i,\theta)} \quad (10)$$

$$\frac{di}{dt} = \frac{-V_{dc} - \frac{d\lambda(i,\theta)}{d\theta}\omega - i * R}{L(i,\theta)} \quad (11)$$

Simulations in Figures 25 (a) through (c) show that at certain speeds the supply voltage is incapable of meeting the slew rate with the available 12 V supply. The back-emf also increases with increasing current magnitude. By comparing Figures 25(b) and (c) it can be seen that the 12V supply is incapable of meeting the slew rate demand at 1-Nm but it can do so at 0.3-Nm. In order to ensure the demand is met at all speeds, the supply voltage needs to increase to accommodate back-emf build up according to the torque-speed characteristics.

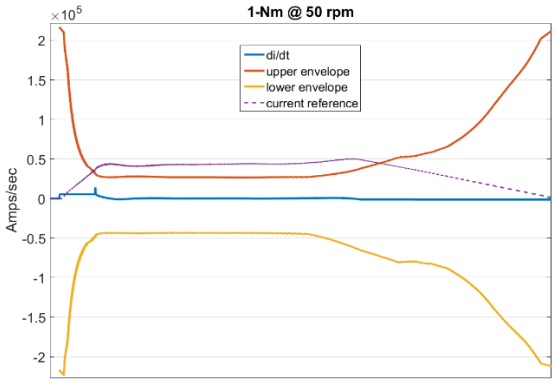

Figure 25 (a): Simulations of di/dt demand and upper/lower voltage supply limits outputting 1-Nm at 50 RPM

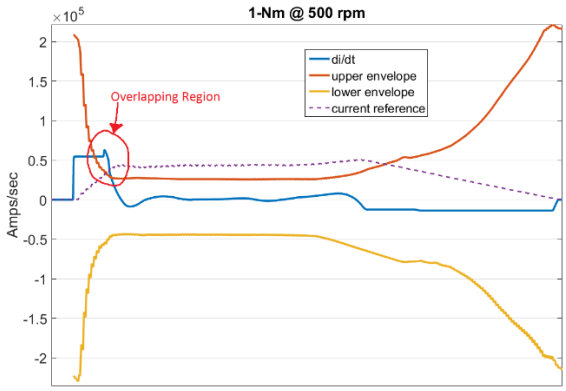

Figure 25 (b): Simulations of di/dt demand and upper/lower voltage supply limits outputting 1-Nm at 500 RPM

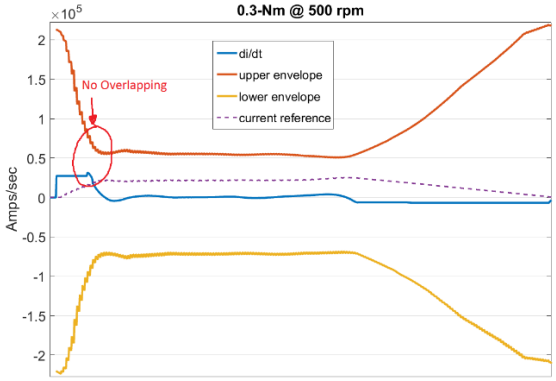

Figure 25 (c): Simulations of di/dt demand and upper/lower voltage supply limits outputting 0.3-Nm at 500 RPM

At certain speeds, there are other additional factors influencing the ripple magnitude. A closer comparison between reference and measured current at 500 and 700 RPM can help reach a conclusion. Reference and measured current at these two different speeds and corresponding torque ripples are shown in Figures 26(a)-(d). Comparing Figure 26(a) with Figure 26(c) it can be seen that current following performance is significantly better at 500 RPM than that at 750 RPM. Though there is the issue of sampling rate, Figure 26(a) and Figure 26(c) are taken at relatively similar mechanical speeds, only differing by one and a half times lower samples per cycle at 750 RPM.

If torque ripple performances at these two speeds are compared, it can be observed that the ripple at 500 RPM is nearly twice the ripple as the one observed at 750 RPM. This clearly contradicts the idea that torque ripple performance degrades with increasing speeds due to a poor current following. In fact, 500 RPM resulted in the worst torque ripple performance among the tested torque data. A thorough analysis of the ripple performance is needed to identify the true contributor.

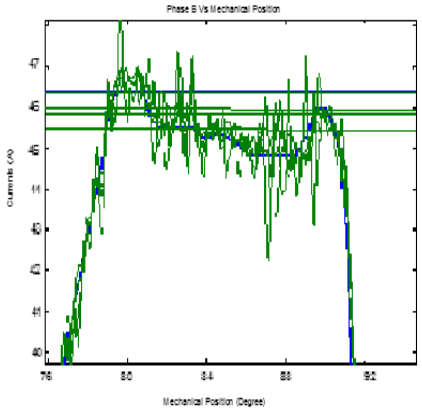

Figure 26 (a): Reference and measured current at 500 RPM.

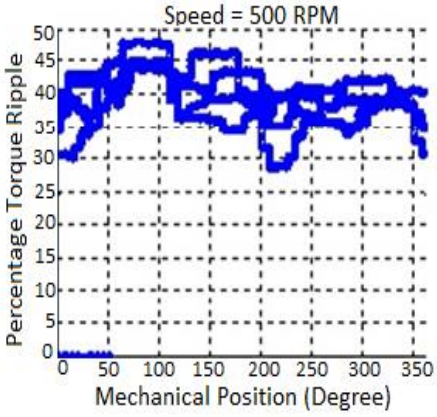

Figure 26 (b): Percentage torque ripple at 500 RPM.

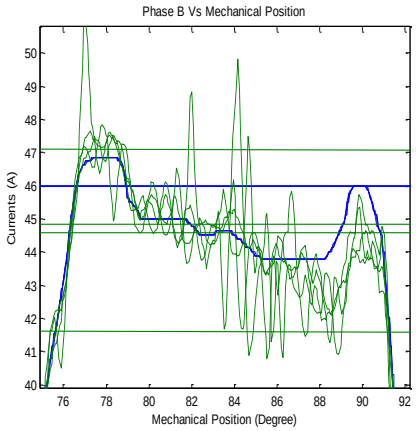

Figure 26 (c): Reference and measured current at 750 RPM.

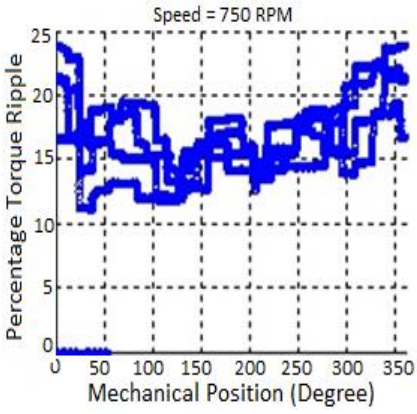

Figure 26 (d): Percentage ripple at 750 RPM.

3.1.4 System Resonance

Torque ripple in SRM shows some distinctive pattern which can be effectively identified when presented in frequency domain. Depending on the rotational speed, a certain harmonic

contribution dominates at certain frequencies. When scaled by mechanical speed, the order of the harmonic contributions is found which eventually result in dominant ripple contribution(s) at certain harmonic orders.

Harmonic analysis of torque ripple at different rotational speeds are given in Figures 27 (a)-(d). In the x-axis, both harmonic orders and frequencies are presented. Ripple contribution from electromagnetic torque diminishes at very high order, up to 130th order are taken for computing the filtered torque output. The higher orders arise from torque transducer noise, system vibration etc. and are neglected.

Careful observation of the harmonic component at lower speeds suggest that there are different contributors to torque ripple between 150 - 200 Hz. Since these frequencies correspond to extremely high harmonic order at this low speed, they are simply not creating any effect in the ripple computation. All lower order harmonic components have relatively small magnitudes at lower speeds (10-50 RPM). As we move on to 100 RPM, the 150 – 200 Hz frequency range falls below the 130th order making it no longer negligible for torque ripple computation purposes. As this frequency range moves below the 130th order, the result also shows a simultaneous increase in the magnitude of the 120th order, which had a smaller contribution at lower speeds. This phenomenon is known as resonance. Any harmonic order that overlaps with this natural frequency range is expected to have a large magnification in torque ripple due to the superposition of the natural frequency as well as the existing harmonic order. In Figure 27(d) this resonance overlaps with the 24^{th} order harmonic, significantly increasing the torque ripple magnitude.

The resonant frequencies are dictated by the natural mode frequencies linked to the design and the fundamental operating frequency linked to the rotational speed. The resonance can be avoided by pushing the natural mode frequencies to higher levels and should be addressed during the design stage [15].

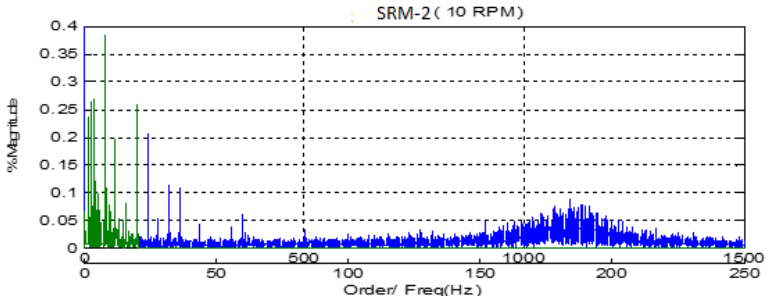

Figure 27 (a):Torque ripple magnitude vs. corresponding harmonic order and frequency at 10 rpm

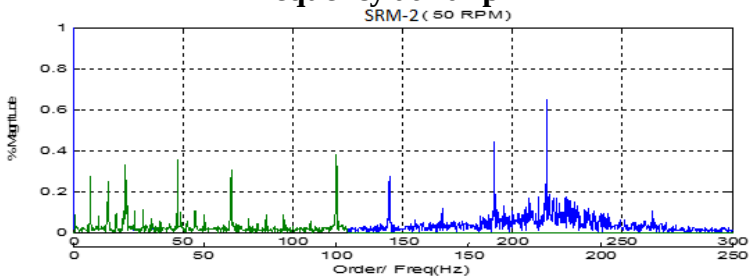

Figure 27 (b):Torque ripple magnitude vs. corresponding harmonic order and frequency at 50 rpm

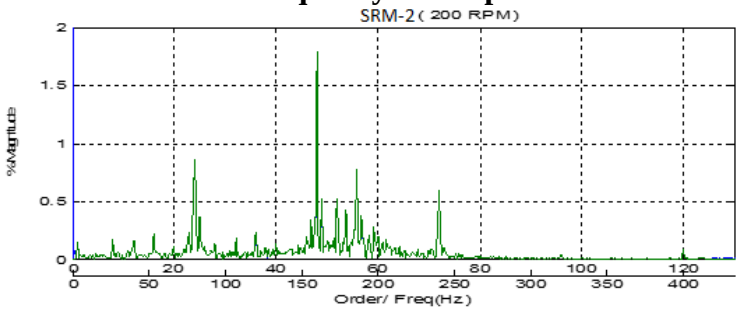

Figure 27 (c):Torque ripple magnitude vs. corresponding frequency and harmonic order at 200 rpm

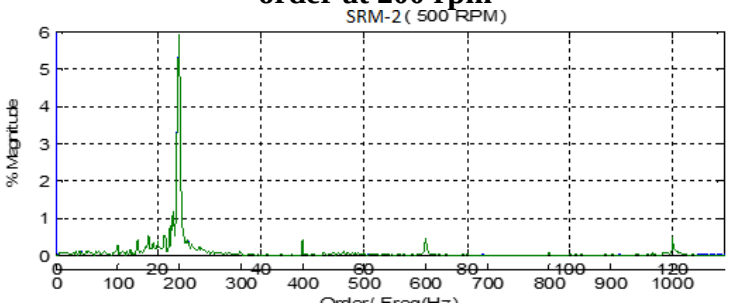

Figure 27 (d):Torque ripple magnitude vs. corresponding frequency and harmonic order at 500 rpm

3.2 Parametric Analysis

Parameters of interest were varied to gain a better understanding of the effects on torque performance. The Matlab/Simulink model of the SRM in addition to the FEA model in Flux2D were used. A new current profile was developed for simulation purposes, maintaining similar levels of torque ripple to that of the experimental runs. The experimental and simulation current profiles are shown in Figure 28 (a) and Figure 28 (b).

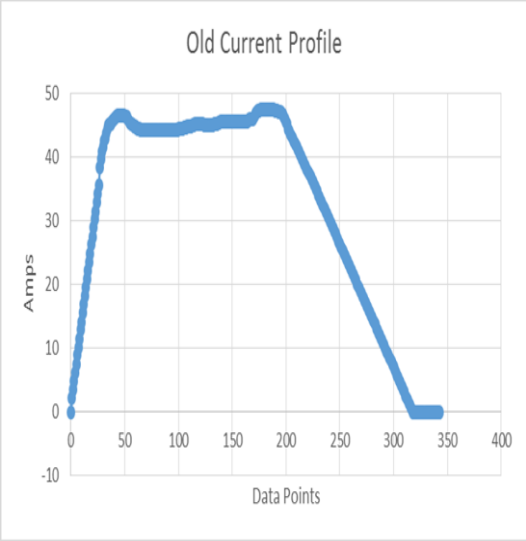

Figure 28 (a): Current profile used for experimental tests on actual SRM

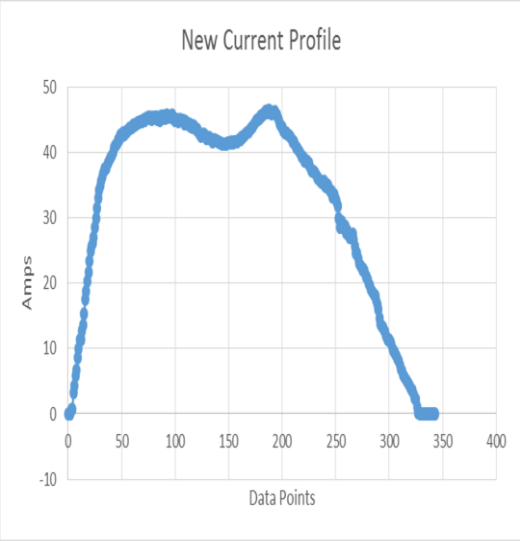

Figure 28 (b): Current profile used for simulation model of SRM

With a simulation model that closely resembles the experimental setup, several machine parameters were varied to measure their effects on the torque output. These included:

- Phase resistance variation caused by manufacturing imperfections as well as temperature variations.
- Rotor eccentricity due to machine construction.
- Voltage supply variation due to changes in battery charge.

3.2.1 Phase Resistance Variation

Two possible scenarios were taken into consideration when varying the phase resistances. Possible manufacturing imperfections could lead to one of the phases, a, b, or c having larger resistances. In order to simulate this the controller phase resistances were kept at the same

value while the phase b resistance of the machine model was varied from 100% to 140 % of its original value 0.1 Ω. The simulation was repeated at 20 RPM as well as 500 RPM to observe its effect at lower and higher speeds. The results are shown in Figure 29 (a) and Figure 29 (b) below.

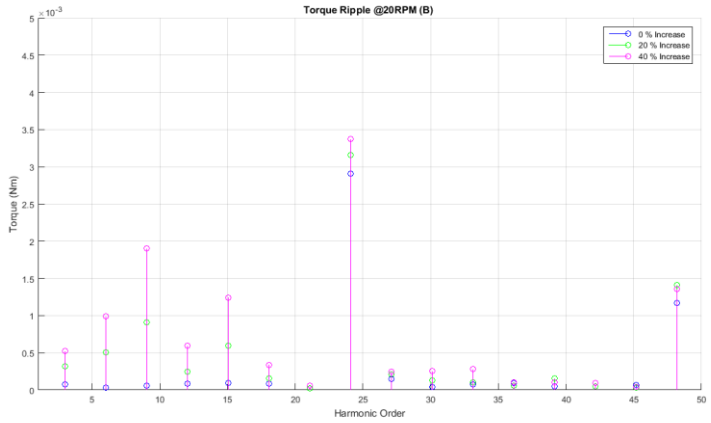

Figure 29 (a):FFT at 20 RPM measuring phase b resistance variation.

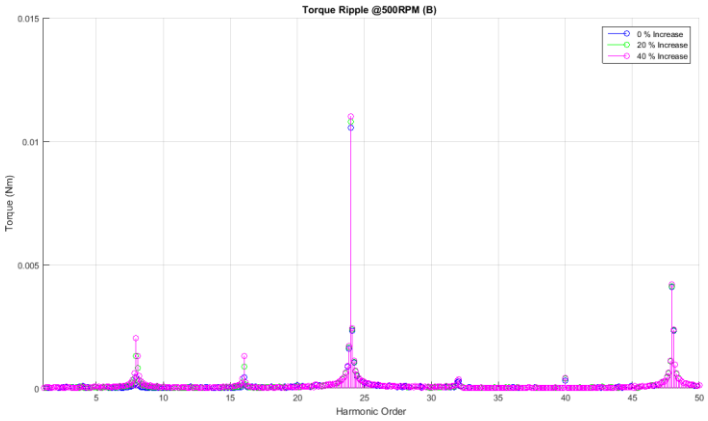

Figure 29 (b): FFT at 500 RPM measuring phase b resistance variation.

Increasing the phase b resistance shows an increase in 8th, 16th, 24th and 48th order harmonics. The magnitude of ripple due to resistance increase in phase b is higher at 500 RPM compared to 20 RPM. As a result we can assume that as speed increases, so will the effect of an increasing resistance due to manufacturing imperfections.

In the second scenario, an increase in the resistances of all phases due to temperature rise is considered. According to T.J.E. Miller, there is a 20% rise in resistance value for every 50^0 C rise [3]. Assuming a temperature range of 20^0C - 120^0C, a corresponding 0% - 40% increase in resistance values will occur. The results are shown in Figure 29 (c) and Figure 29 (d) below.

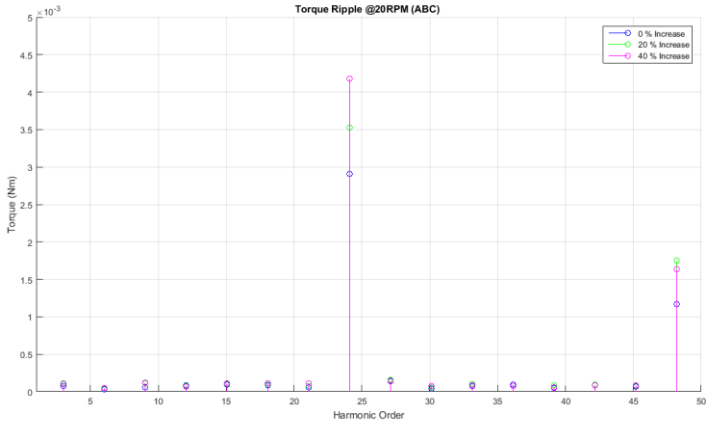

Figure 29 (c): FFT at 20 RPM measuring phase abc resistance variation.

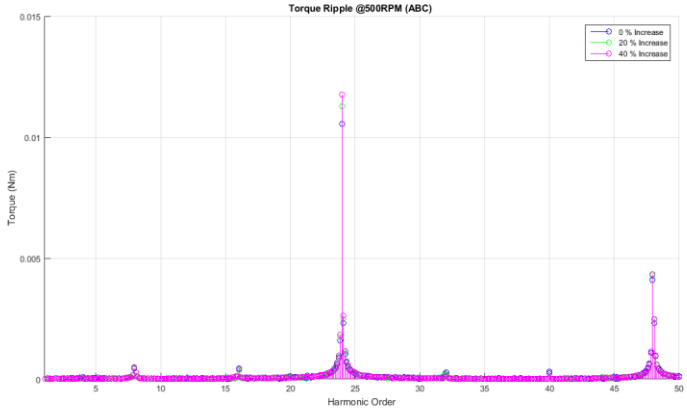

Figure 29 (d): FFT at 500 RPM measuring phase abc resistance variation.

As is shown in the figures above, the magnitude of the torque ripple increases at higher speeds. Another important distinction to make is that the 8^{th} and 16^{th} order harmonics do not contribute as much to the torque ripple in the scenario where all phase resistances are varied. Referring

to Figures 29 (a) and (b)**,** a more noticeable contribution to the torque ripple from the 8th and 16th order is observed, in comparison to Figures 29 (c) and (d). The results are what is expected from a phase-phase variation. As discussed previously, a current gain variation amongst the phases results in an increase in the 8th and 16th order torque ripple contribution.

3.2.2 **Rotor Eccentricity**

Rotor eccentricity describes rotor placement that is not perfectly aligned with the center of the stator. The result of rotor eccentricity is a non-uniform air gap distribution which can lead to variations in phase inductances. In order to test the effects of rotor eccentricity, FEA software Flux2D was used. A shift in the rotor center position was applied to the model. The rotor position was displaced by 30% and 50% of the model's air gap length. In Figure 30, the flux linkage of phases b and c are plotted over one electrical cycle.

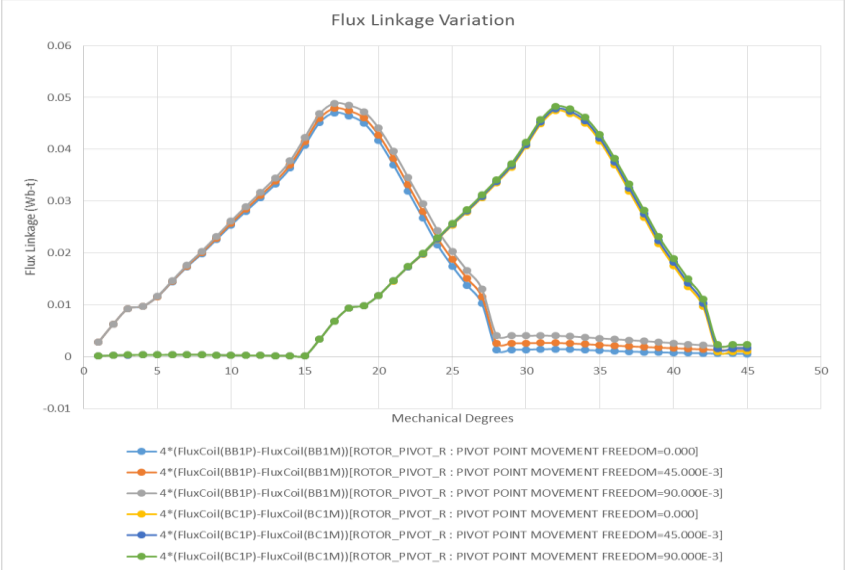

Figure 30: Flux linkage of phase b and c over one electrical cycle (45 mechanical degrees)

In Figure 30 above, the flux linkage is plotted for phases b and c, while varying the rotor eccentricity from an ideal alignment to a shift of 50% of the air gap length. The results show that flux-linkage varies from phase b to phase c, causing a non-uniform flux-linkage distribution among the phases. Furthermore, the amount of flux-linkage with a phase also

varies with the rotor poles. Since rotor eccentricity is applied arbitrarily, the displacement may coincide with a particular stator pole and thus may have a larger effect at that point of rotation. In Figure 30 below, the FFT at 1000 RPM is shown as we applied the rotor eccentricity value of up to 50% of the air gap length.

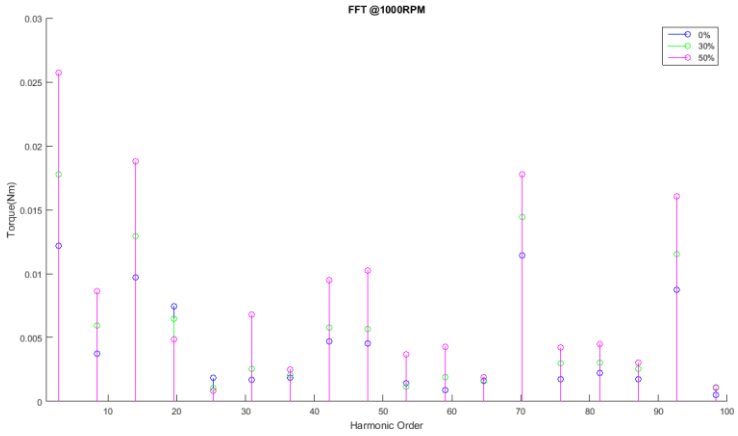

Figure 31: FFT at 1000 RPM with rotor eccentricity applied, from 0% to 50% of air gap length.

The FFT result show an increased contribution to the torque ripple from the 8^{th} and 16^{th} order harmonics as the eccentricity increases. This is expected because as observed in Figure 30, the phase to phase variation increases with increasing rotor eccentricity.

3.2.3 **Voltage Variation**

The value of the supply voltage applied to the SRM is 12 V. Factors such as temperature changes and battery aging can lower the battery charge and thus reduce the available supply voltage. At the same time, increasing the available supply to a reasonable amount and comparing it with a less than ideal supply can provide a better understanding of its influence on phase current following and torque performance. Using the Simulink model of the SRM, the applied voltage was varied from 8V to 16V while running the machine at speeds ranging from 20 RPM to 200 RPM. The results from varying the voltage supply at different speeds are shown in Figures 32 (a) through (h).

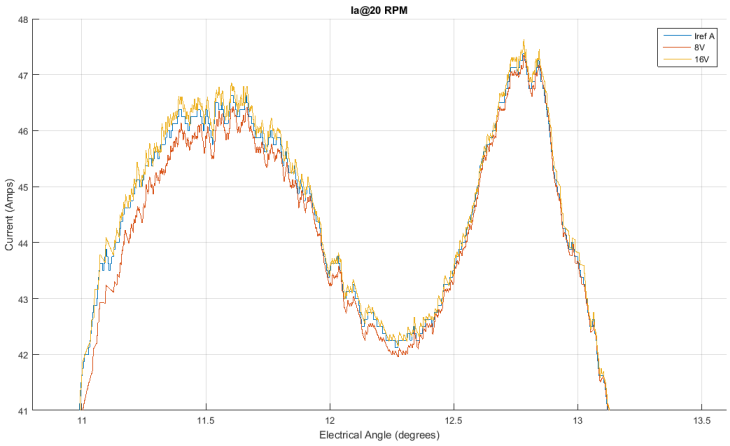

Figure 32 (a): Reference current plot compared to phase current with 8V and 16V battery supplies at 20 RPM.

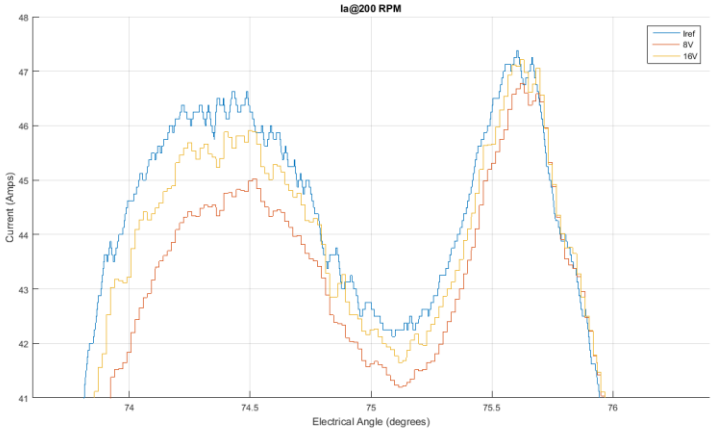

Figure 32 (b): Reference current plot compared to phase current with 8V and 16V battery supplies at 200 RPM.

In the figures above it is clear that the reference current is more accurately followed at lower speed. It is also evident that at both speeds, applying 16V as opposed to 8V leads to a closer following of the reference current profile. This is shown in Figures 31 (c) and (d) below, where the current error is plotted at 20 RPM and 200 RPM, while varying the voltage supply from 8V – 16V.

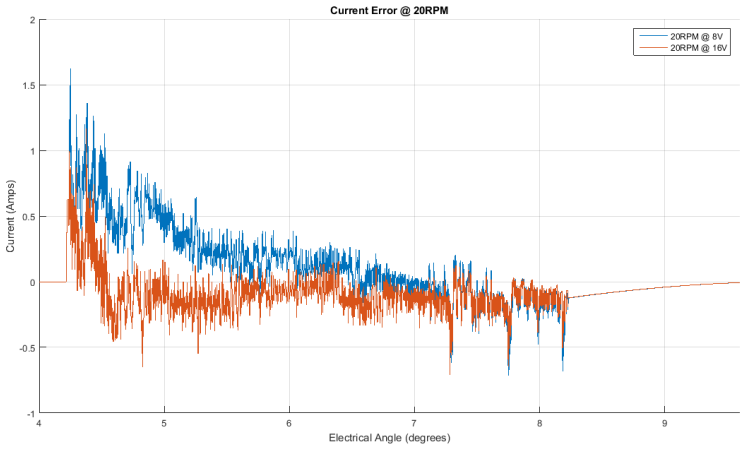

Figure 32 (c): Current error with 8V and 16V supplies at 20 RPM.

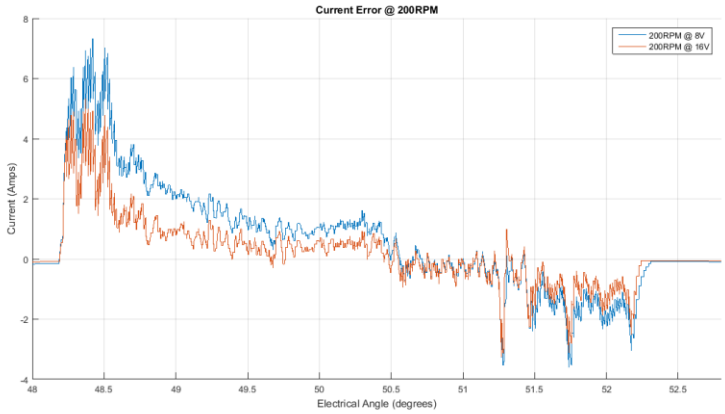

Figure 32 (d): Current error with 8V and 16V supplies at 200 RPM.

The figures above show that at higher speeds the magnitude of current error increases but the 16V supply maintains a smaller current error at both speeds. Next the torque error was measured at 20 RPM and 200 RPM with 8V and 16V supplies. The results are presented in Figures 32 (e) through (f) below.

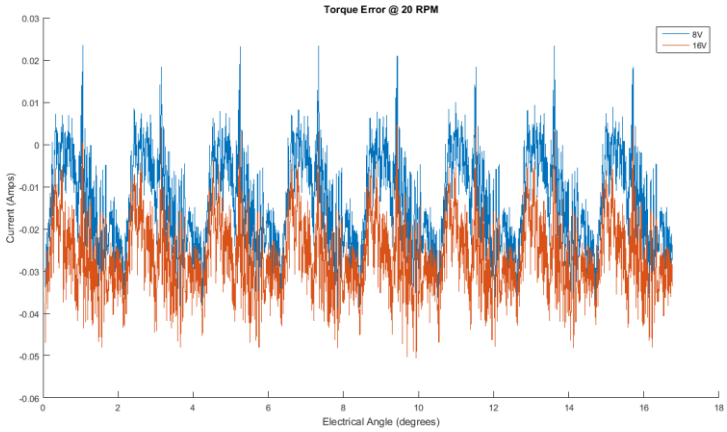

Figure 32 (e): Torque error with 8V and 16V supplies at 20 RPM.

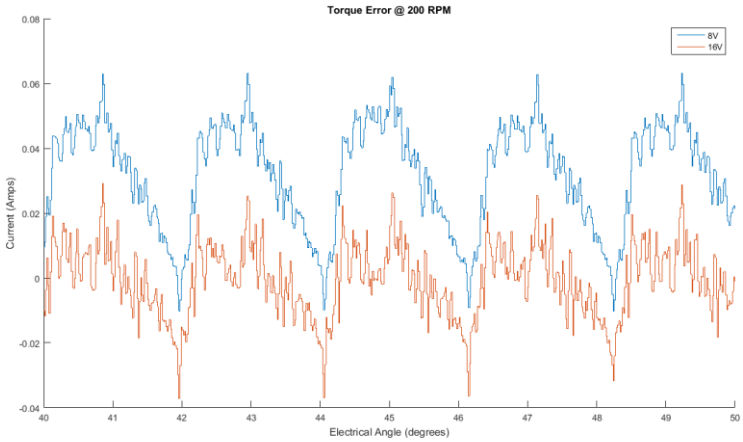

Figure 32 (f): Torque error with 8V and 16V supplies at 200 RPM.

It is evident that increasing the speed will also increase the magnitude of torque error as occurred with the current error. At the same time a higher supply voltage helps decrease the torque error at both speeds. The torque FFT was taken at both 20 RPM and 200 RPM. The results are presented in the Figures 32 (g) and (h) below.

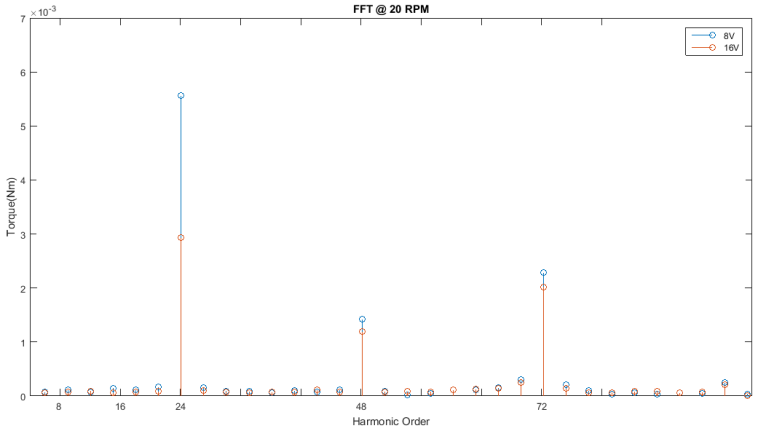

Figure 32 (g): Torque FFT at 20 RPM with 8V and 16V supplies.

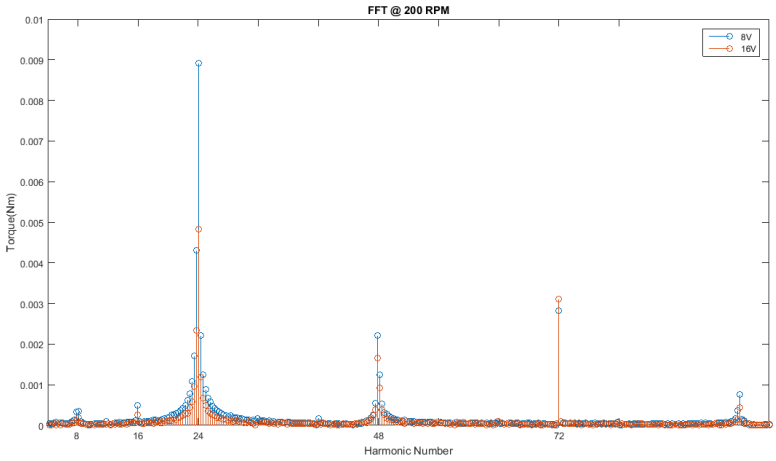

Figure 32 (h): Torque FFT at 200 RPM with 8V and 16V supplies.

From the FFT plots, it can be observed that the 24th order is dominant. Previously it was established that the 24th order is more closely associated with position error and current following inability. Since position error and resonant frequencies are not simulated in the Simulink model of the machine, we can attribute the 24th order to the current following error. As expected, the phase current deteriorates at higher speeds giving rise to higher magnitude ripples at the 24th order harmonic. One way to mitigate this is to increase the supply voltage. As shown in the results the magnitude of the 24th order is reduced in both cases.

Chapter 4 Synchronous Reluctance Machine Evaluation for EPS

Due to the difficulties faced with the SRM in terms of low torque ripple performance, other motors were considered for automotive power steering applications. An alternative is the synchronous reluctance machine (SynRM). The remainder of Chapter 4 includes a discussion on the working principles of the synchronous reluctance machine and an introduction to a new potential design for automotive EPS use. In order to test and measure torque and other outputs of the SynRM model, FEA simulation software Flux2D was used. Using the software, machine parameters were varied while measuring the torque performance. Parameters of interest were adjusted in order to maximize torque ripple performance. Lastly, the SynRM was properly sized to meet SRM size specifications. The final design meets the EPS criteria of maintaining torque ripple below 5%.

4.1 Synchronous Reluctance Machine Fundamentals

Like the SRM, the SynRM works on the principle of reluctance torque and no permanent magnets are required. Unlike the SRM, the SynRM can operate with a conventional induction machine stator. The SynRM is supplied with 3-phase sinusoidal waveforms and it doesn't require a specially designed inverter like in the SRM. The rotor is designed with flux barriers of various shapes and sizes in order to maximize reluctance torque output. In addition to having no permanent magnets, it can achieve high power densities with respect to its size, and maintains a higher torque output/iron loss when compared to the Induction Machine. [12][13] The SynRM torque output is defined in equation 12.

$$T_e = \left(\frac{3P}{2}\right) * \left(L_d - L_q\right) * i_{dm} * i_{qm} \quad (12)$$

By looking at equation 12, it is evident that in order to maximize torque production L_d(d-axis inductance) needs to be maximized and L_q (q-axis inductance) minimized. In order to obtain a high Ld/Lq ratio, the rotor must be designed in such a way to obstruct the flux path through the quadrature axis (q-axis) while maintaining the flux flow through the direct axis (d-axis). In Figure 32 below, the flux barriers (air gaps) are shaped to obstruct flux flow from the shaft center to the edge of the rotor, along the q-axis.

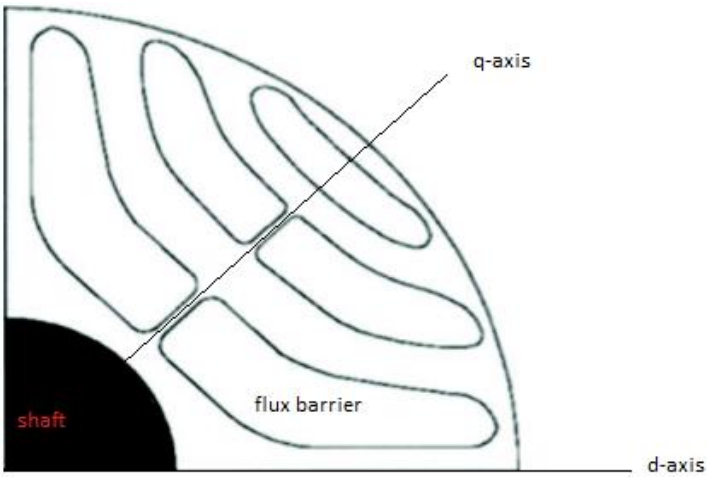

Figure 33: SynRM rotor lamination showing q and d-axis directions.

4.1.2 Synchronous Reluctance Machine Design

In the new SynRM design the aim was to improve torque ripple performance for automotive EPS application. A 36 slot, commercially available induction machine stator model was used. The initial rotor design consisted of triangular flux barriers in the rotor. The rotor design was later modified. Figure 34 below shows ¼ of the SynRM model prior to any changes done to it.

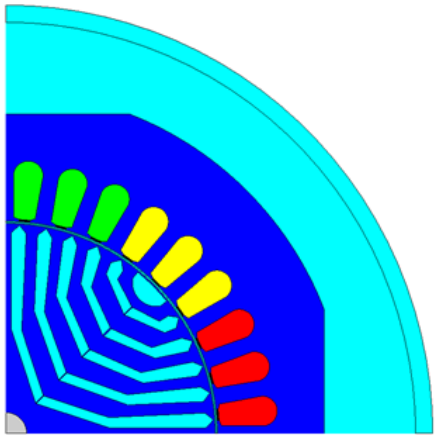

Figure 34: ¼ of SynRM Flux2D model.

The different colors represent the three phase coils and face regions including air gap, stator and rotor core, and rotor shaft. Table 1 below includes the initial SynRM dimensions.

Table 1: SynRM Dimensions	
Specifications	**Size**
Stator Slot Number	36
Pole Number	4
Air Gap	0.5 mm.
Shaft Radius	5 mm.
Rotor Radius	50.15 mm.
Inner Stator Radius	50.650 mm.
Outer Stator Radius	81.75 mm.
Power Output	735 Watts
Voltage Output	266 VRMS
Current	1.55 ARMS
Number of Turns	240

The aim was to reduce the torque ripple output to below 5%. The approach taken was through geometric modifications to the rotor.

4.2 **Rotor Barrier Designs and Parameter Variations**

Since rotor designs in SynRM tend to be more unique to the application purpose, a strong focus was placed on the rotor geometry to achieve good torque performance [12]. The initial model was designed with five triangular barriers/pole. An alternative circular flux barrier shape was introduced. Figure 35 below depicts the two barrier designs.

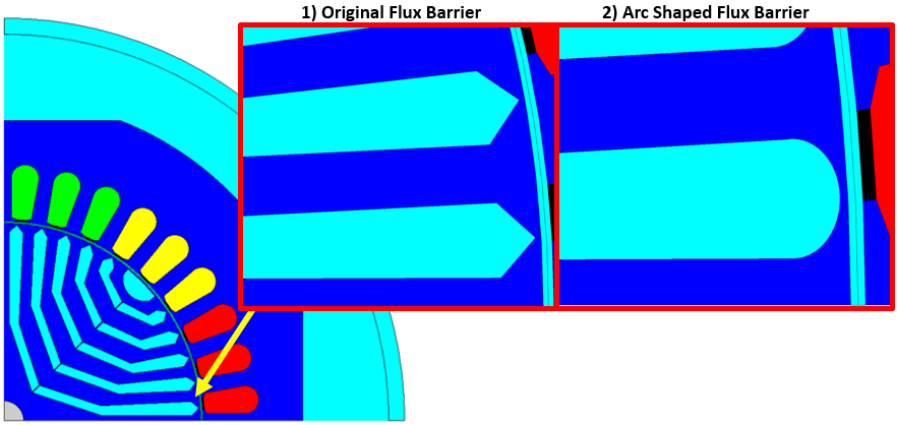

Figure 35: Original triangular shaped flux barrier design and modified circular arc shaped flux barrier.

Geometric rotor parameters were selected and varied to measure their effects on average torque output as well as torque ripple efficiency. The aim was to maintain the torque ripple output below 5% without sacrificing more than 10% of average torque production. Figures 36 (a) and (b) depict the parameters selected.

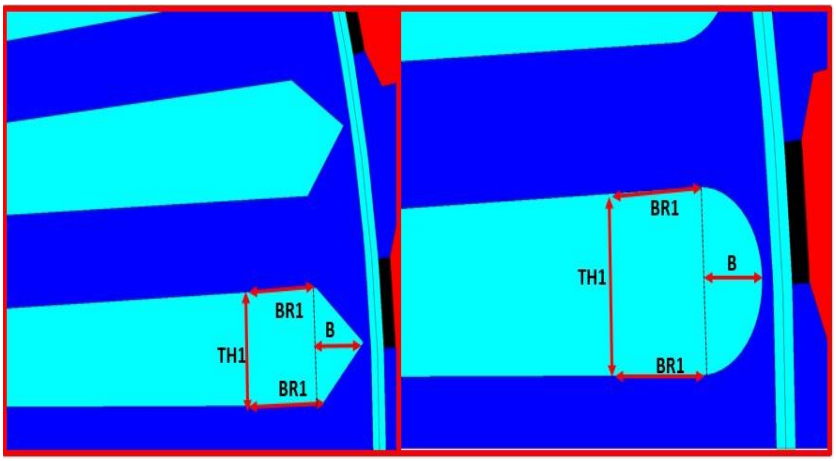

Figure 36 (a): B (bridge length), BR1 (barrier radius), and TH1 (barrier thickness) varied in triangular design and arc shaped design flux barriers.

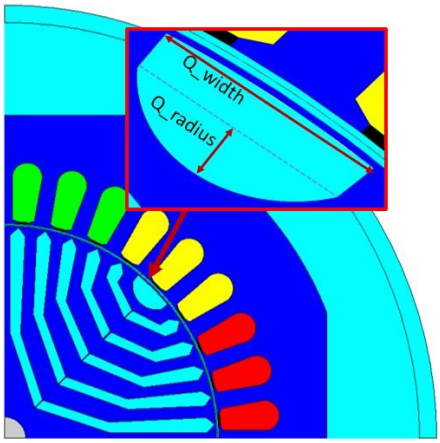

Figure 36 (b): Q-width and Q-radius varied in central flux barrier.

4.1.3 Parameter Variation Results

Using FEA software Flux2D, the SynRM model was modified based on parameters of interests. The simulations were done at a speed of 1800 RPM using ¼ of the machine model. Balanced, three phase sinusoidal currents were applied while the load angle remained constant

at 26 °. It can be seen from the results in Figures 37(a)-(h) below that certain parameters affected torque production more than others.

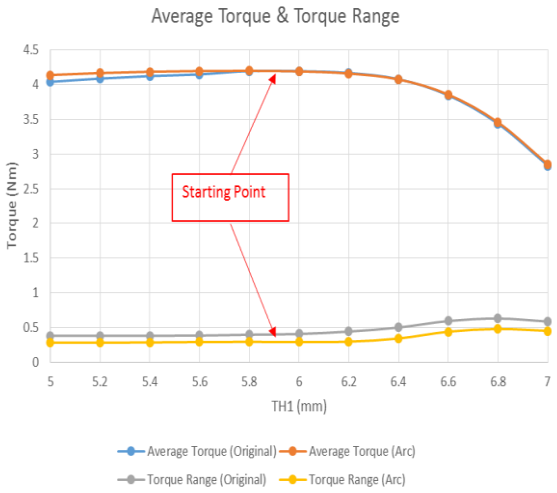

Figure 37 (a): Average Torque and Torque Range output from TH1 variation

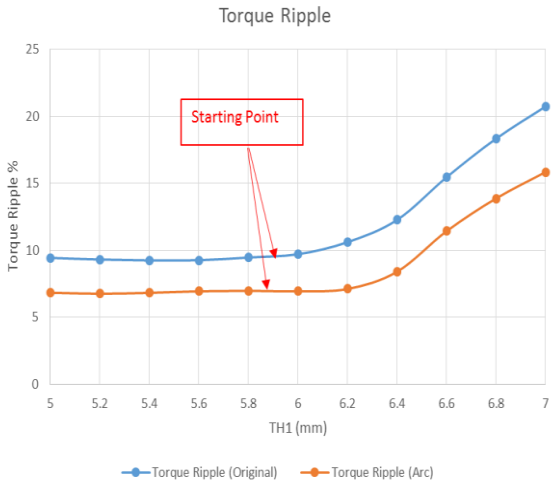

Figure 37 (b): Torque Ripple output from TH1 variation

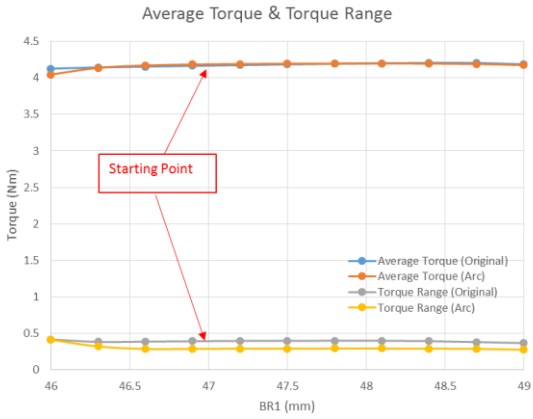

Figure 37 (c): Average Torque and Torque Range output from BR1 variation

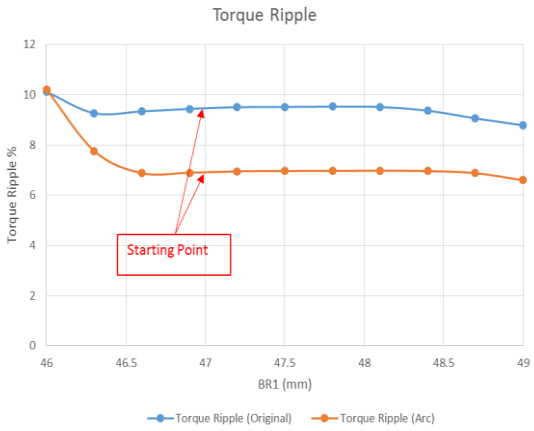

Figure 37 (d): Torque Ripple output from BR1 variation

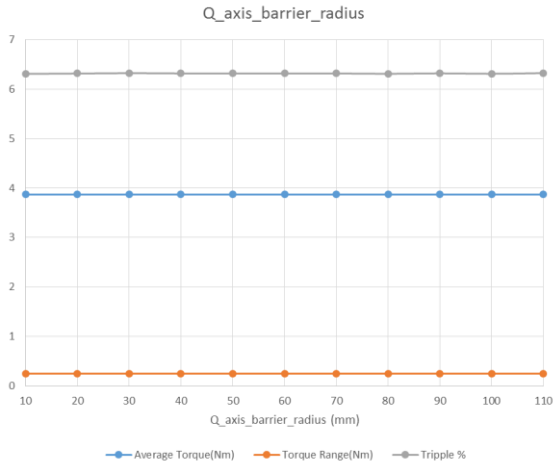

Figure 37 (e): Average Torque, Torque Range, and ripple output from q-axis radius variation.

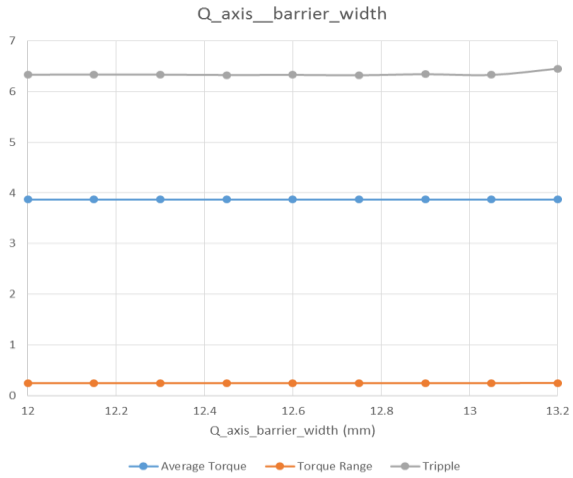

Figure 37 (f): Average Torque, Torque Range, and ripple output from q-axis width variation.

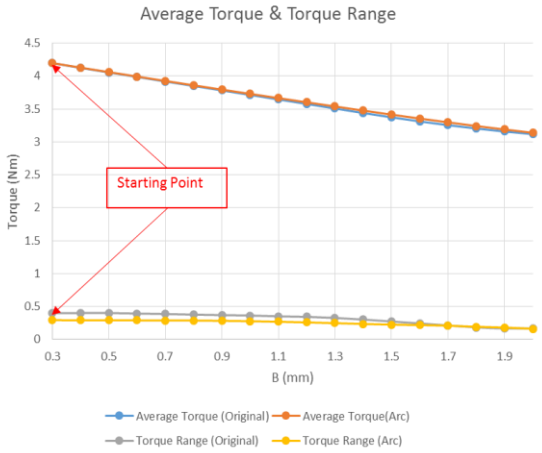

Figure 37 (g): Average Torque and Torque Range output from B variation

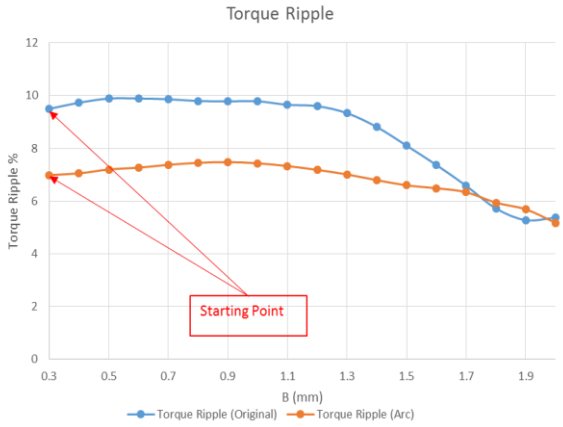

Figure 37 (h): Torque Ripple output from B variation

Q-axis radius and width variation had the smallest effect in terms of torque, torque range, and torque ripple output. Flux barrier thickness (TH1) and barrier radius (BR1) did have a considerable effect on the torque output and ripple. The bridge length (B) between the flux barrier and air gap had the greatest effect on the torque output and torque ripple amongst the parameters. The results demonstrate that the initial parameter values already produced

sufficient torque with relatively small torque ripple. One result that remains consistent is the improved torque ripple performance using arc barrier design. Referring to Figure 37 (h), a 3% drop in torque ripple is achieved by implementing arched barriers. A possible explanation for this could be a smoother edge transition in the arc shaped barrier. Because the triangular barrier design has an abrupt edge, the arc design may redirect the flow of magnetic flux more efficiently in the rotor core. This is shown in Figures 38(a)-(b) below.

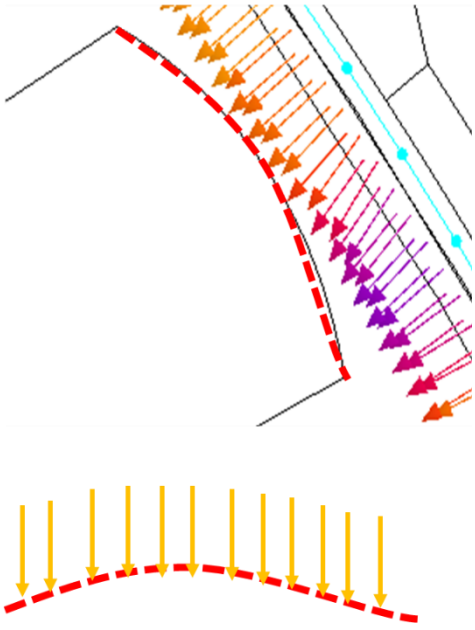

Figure 38 (a): Magnetic flux with arc shape barrier

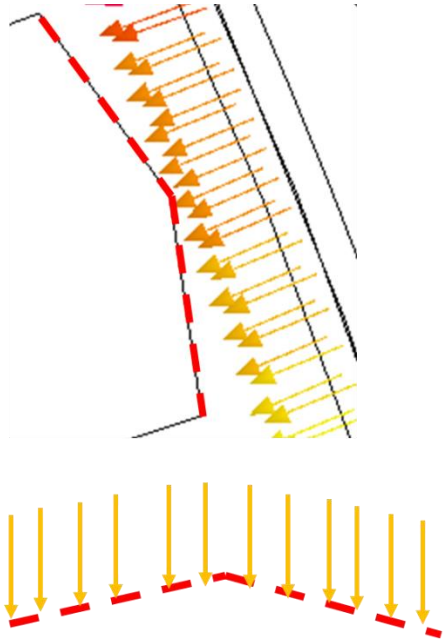

Figure 38 (b): Magnetic flux with triangle shape barrier

4.1.4 **Rotor Skewing**

Another method to improve torque ripple performance is to skew the rotor laminations. The amount of skewing is measured based on the degree of rotation from the top to the bottom of the lamination stack. From research done on SynRMs, Bomela and Kamper, suggest that for a 36 slot machine, a 10 degree rotor skewing or a shift of a single slot pitch, provides sufficient ripple reduction with minimal effect on average torque output [14]. Furthermore, in order to accurately test rotor skewing in FEA, the rotor is divided into 5 parts each shifted by $1/5^{th}$ of skewing angle [14]. The skewing angle was varied from 5 to 20 degrees with

increments of 5 degrees. After the torque ripple minima was found to exist in the 10-15 degree range, another sweep was performed in the latter range with 1 degree intervals. Figure 39 below shows the results measured from the rotor skewing.

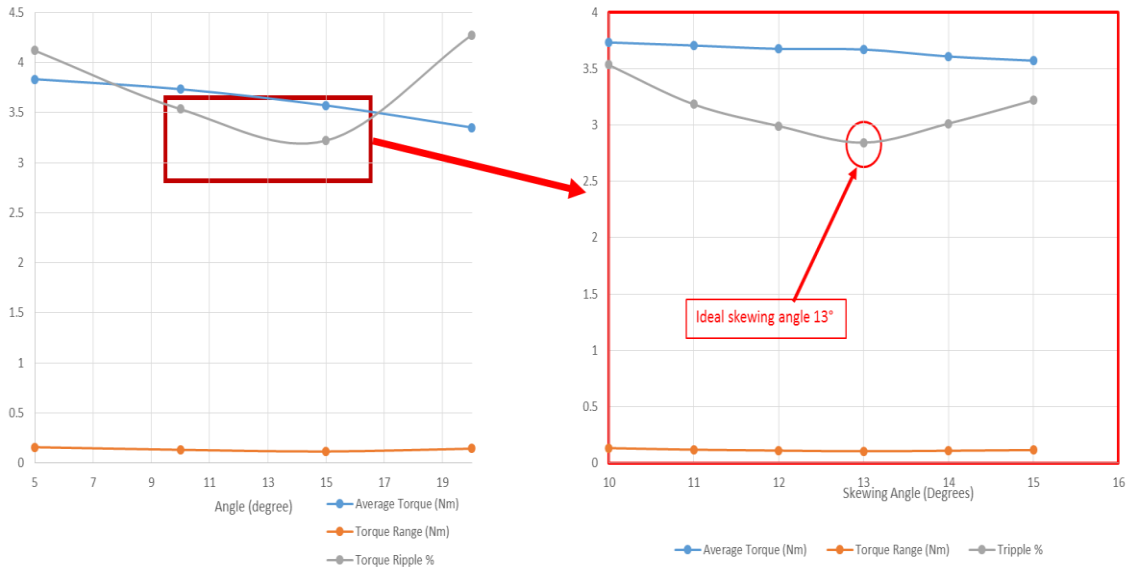

Figure 39: Rotor skewing from 5-20 degrees (left) and 10-15 degrees (right).

An ideal skewing of 13 degrees provides the lowest torque ripple output. The following parameters values were set for the final SynRM design, while Figures 40 (a) and (b) display the original and modified rotor design.

- Bridge Length (B) of 0.7 mm
- Flux Barrier Radius (BR1) of 49 mm
- Flux Barrier Thickness (TH1) of 5.8 mm
- Rotor Skewing of 13 degrees

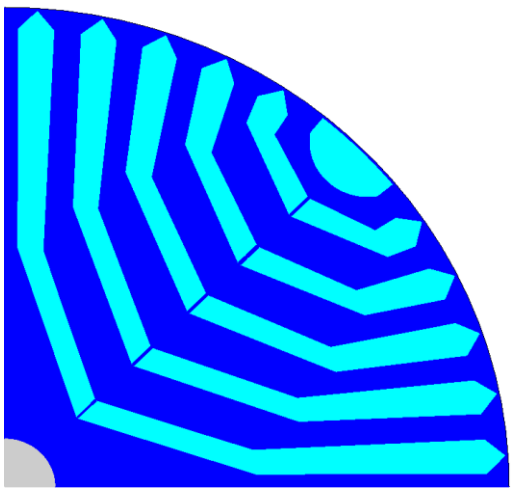

Figure 40 (a): Original rotor design

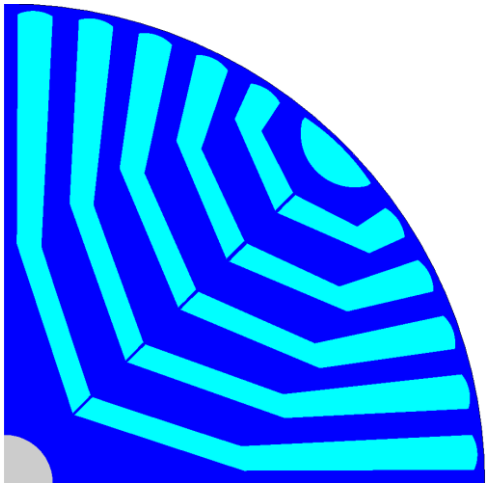

Figure 40 (b): Modified rotor design

4.3 **SynRM Benefits, Design Constraints, and Targets**

Some of the benefits of using a SynRM are as follows:

1) The SynRM has no PMs and has a simple and robust design structure. In this aspect, SynRM is as good as SRM. The SynRM can also operate with an induction machine stator, as is the case for the design presented above.
2) The SynRM has sinusoidal waveforms and vector control can be used for improved torque ripple performance. Vector control is a well-developed high performance control method that is widely used for PMSMs and induction machines. Vector control algorithms are well established and easier to implement than nonlinear SRM controls and could also be more effective for this application. For the SRM, a specific current profile and an accurate position sensor are needed to obtain good torque ripple performance. In SynRM we don't have to worry about developing a specific current profile. Furthermore, a sinusoidal current profile could be easier to follow at higher speeds in comparison with the pulse shaped one used in the SRM. A high resolution position sensor is required for SynRM as well. The sensitivity to position error in SynRM compared to SRM needs to be evaluated.
3) SynRM uses a standard 6-switch inverter with conventional PWM modulation techniques. This adds to the simplicity of the machine controller.

The design constraints based on the torque performance requirements are discussed below.

1) Maintain similar dimensions. Since size is another importance factor for EPS applications, the machine dimensions, excluding stack length, were kept the same as the SRM. Due to lowered power density in SynRM, stack length was increased accordingly to provide sufficient torque output.
2) Maintain similar current density as the SRM. Since machine sizes are the same, the same current density of approximately 20 Amps/.mm^2 is maintained
3) Use the same 12V battery voltage. It was taken into consideration that the only available supply voltage is the 12V car battery supply. As a result, the SynRM was designed to meet the 12V DC requirement.
4) Follow the same torque-speed characteristics envelope. The aim was to recreate the same torque-speed characteristics since the original SRM was designed to fit a specific criteria set for EPS applications.

The SynRM targets for EPS application included:

1) Reduce torque ripple while maintaining similar torque-speed output as the SRMs.
2) Maintain minimum stack length that satisfies torque requirement as well as similar motor dimensions to the SRM design.
3) Implement sinusoidal waveforms for easier controls

4.3.1 **Synchronous Reluctance Machine Resizing**

After rescaling the SynRM to SRM dimensions, another sweep of the load angle and rotor skewing was performed to achieve optimal torque performance. Figures 41 (a) and (b) show the new optimal load angle and rotor skewing angle.

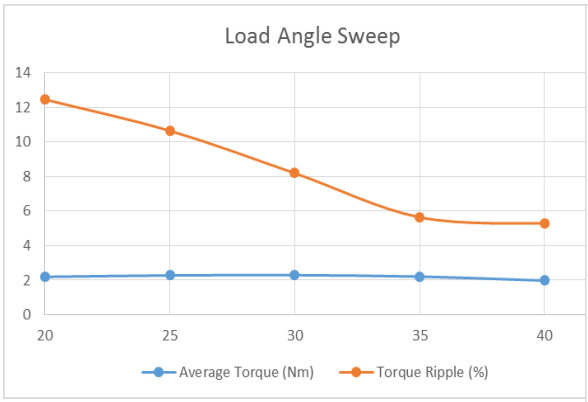

Figure 41 (a): Load angle sweep of resized SynRM

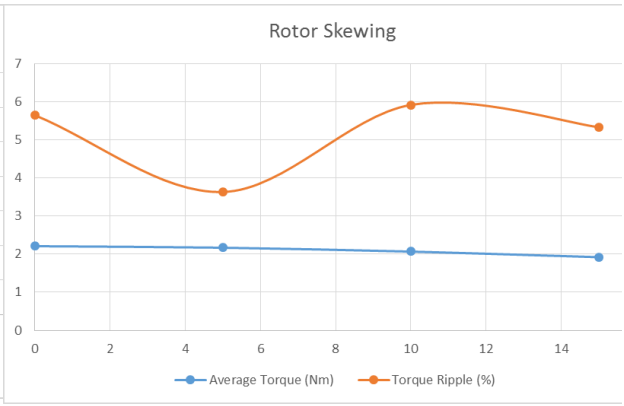

Figure 41 (b): Rotor skewing sweep of resized SynRM

From the Figures above it is shown that the optimum load angle for the resized SynRM is 35 degrees and the skewing angle is 5 degrees. The results of the torque and voltage waveforms are shown in Figures 41 (c) and (d) below.

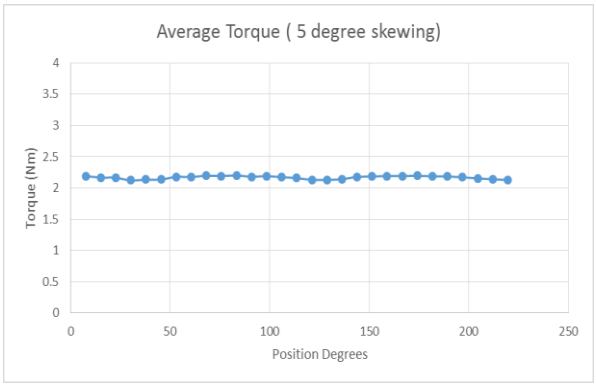

Figure 41 (c): Average torque output after skewing

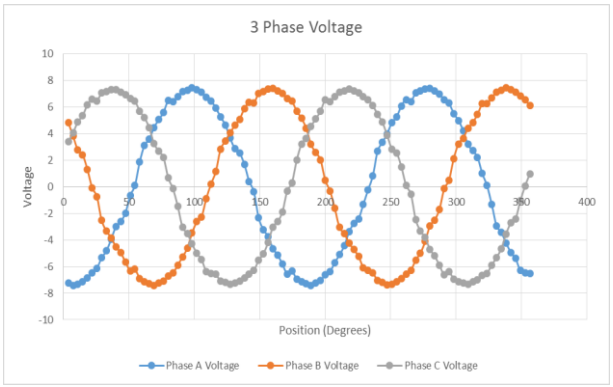

Figure 41 (d): 3-phase sinusoidal voltage waveforms

After the rotor designed was finalized, a comparison was performed with the SRM. Table 2 below includes the machine characteristics and performance results of the SRM as well as the newly designed SynRM.

Table 2: SRM and SynRM Performance Comparison		
	SRM	**SynRM**
Power	251 W	230 W
Torque (rated)	2.4 Nm	2.20 Nm
Speed (base speed)	1000 rpm	1000 rpm
Torque Ripple (%)	~5%	3.6%
Voltage Supply	12 V	12 V
Current Density	22 Amps/mm^2	20 Amps/mm^2
Current RMS	20 Amps	9 Amps
Number of Stator Slots	12	36
Number of Turns/Slot	72	24
Stack Length	32 mm.	44 mm.
Outer Diameter	85 mm.	85 mm.

Interpretation of key results:

- The torque speed specifications for the SRM are maintained with the SynRM design, producing 2.2-Nm at 1000 rpm.
- In comparison to the SRM, the SynRM torque ripple is reduced, with easier control and less stringent requirements for sensor accuracy. Conventional PWM switching as well as induction machine stator can be implemented in SynRM.
- Stack length is 37% larger but acceptable as further improvements to rotor design can be done to reduce stack length to a value closer to the intended size.

The SynRM provides improvement in torque ripple performance with changes applied to the rotor geometry. The power output and torque-speed specifications remained the same as the SRM. Voltage supply requirements remained the same. Since the SRM has higher power density, the stack length increased from 32 to 44 mm in order to compensate for it. Due to the simplified control and easily modifiable rotor geometry, further torque ripple reductions are possible. Although average torque output suffers in comparison to the SRM, increasing the stack length could be done in order to improve the torque performance.

In the SynRM design torque ripple performance was prioritized. Machine geometry and stack length were adjusted accordingly. Mechanical stability of the rotor, barrier bridge thickness, as well as different flux barrier densities were not simulated. ¼ of the optimized SynRM model is depicted in Figure 41 below.

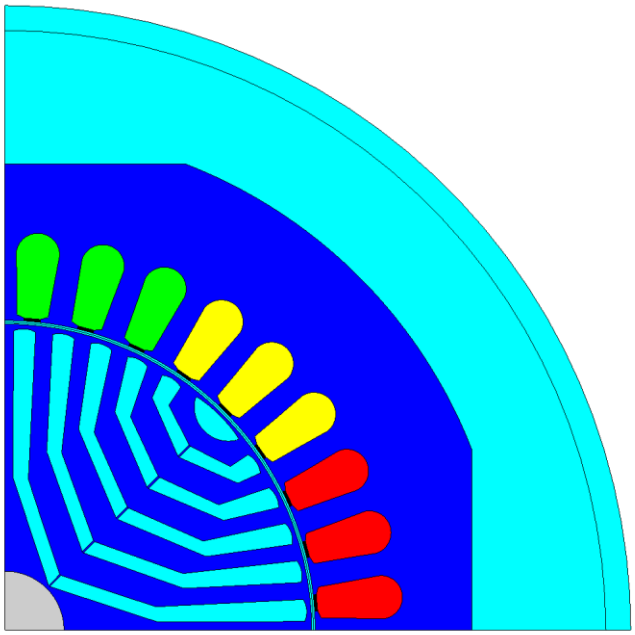

Figure 42: 1/4th of the resized SynRM model

Chapter 5 Conclusions

From previous research, a specially designed SRM was modeled, constructed, and tested for the purposes of automotive power steering. Two identical SRM prototypes were built and experimental tests along with simulations were performed. SRM-1 exhibited good torque ripple performance whereas SRM-2 did not. The experimental data from SRM-2 was collected and analyzed. Results indicated existing errors in the position sensor, current following deterioration with increasing speed, phase to phase variations, as well added ripple due to the natural resonant frequency. Simulations of the SRM model displayed the effects of varying the SRM's phase resistances, rotor eccentricity, and voltage supply. These parameter effects along with errors encountered in experimental tests on the SRM, provide a better understanding of potential issues affecting torque ripple performance.

The SynRM is introduced as an alternative motor for automotive EPS. Advantages include a lack of permanent magnets, ability to use a conventional induction machine stator, as well as standard 6-switch inverter with conventional PWM methods implemented. After geometric modifications were done to the rotor and a resizing of the SynRM model to fit the SRM's sizing criteria was performed, the model showed good torque ripple performance. However, due to the lower power output, the stack length was increased by 37% in order to generate the same rated torque as the SRM. Issues dealing with mechanical stability and noise production were not considered during simulations.

In order to have more accurate results of the SynRM, a Simulink model based on the designed machine and controller should be constructed. If the results are acceptable for EPS applications, a prototype machine should be constructed for experiments. Manufacturing imperfections as well as sensor errors should be simulated and tested in order to obtain more accurate results of torque performance, and be able to compare those results with the SRM.

REFERENCES

[1] Miller, T.J.E. *Electronic Control of Switched Reluctance Machines*. Woburn: Reed Educational and Professional Publishing Ltd, 2001. Print.

[2] Krishnan, R. *Switched Reluctance Motor Drives*. Boca Raton: CRC Press LLC, 2001. Print.

[3] Miller, T.J.E. *Switched Reluctance Motors and their Controls*. Hillsboro: Magna Physics Publishing, 1993. Print.

[4] Mikail, Rajib. "High Performance Control of a Switched Reluctance Machine." Diss. North Carolina State University, 2013. Print.

[5] Jin, Woo Ahn. *Torque Control.* InTech, 2011. Print.

[6] Bianchi, Nicola, and Silverio Bolognani. "Design of a Fault-Tolerant IPM Motor for Electric Power Steering." *IEEE Transactions on Vehicular Technology*, Vol.55, No.4 July (2006): 1102 – 1111. IEEE online. Web.

[7] Rodriguez, F, E. Uy, and A.Emadi. "Brush-Less DC Motor Drive for Steer-By-Wire And Electric Power Steering Applications." 535 – 541. Web.

[8] Torrey, A. David, and James. M. Kokernak. "Power Steering: Brushless DC or Switched-Reluctance?" *Power Electronics Technology*, August 2002. Web.

[9] “Resolver Fundamentals.” Delta Computer Systems. deltamotion. Delta Computer Systems, Inc. 2005 – 2014.

[10] Prentice, Michael. ”Resolvers 101: Understanding the Basics.” *Dynapar Industry White Papers:* 1-4.Web.

[11] Fahimi, B., J.P. Johnson, and M.Ehsani. “Artificial Intelligence Approach to Controlling SRM Drives with Manufacturing Imperfections.” *IEEE*. (1996): 623-628. Web.

[12] Promaidis, Ioannis Ch., Dionysis V. Spyropoulous, and Epaminondas D.Mitronkas. “An Alternative for All-Electric Ships Applications: The Synchronous Reluctance Motor.” *Advances in Power Electronics* Volume (2013): 1-7. Web.

[13] Husain, Iqbal. “Various Synchronous Machines dq Model.” North Carolina State University. Centennial Campus, Raleigh, NC. Fall 2015. Lecture.

[14] Bomela, Xola. B, Maarten J.Kamper. “Effect of Stator Chording and Rotor Skewing on Performance of Reluctance Synchronous Machine.” *IEEE Transactions on Industry Applications.* Vol. 38, No.1. January/February (2002): 91-100. Web.

[15] “Resonance.” Wikipedia. 25 December 2015. Web. 20 January 2016.